https://doi.org/10.5194/egusphere-2026-4117
Preprint. Discussion started: 15 July 2026

The boundary of nighttime ozone chemical equilibrium as an indicator of local chemistry disturbances in the polar mesopause region

Mikhail Yu. Kulikov[1], Mikhail V. Belikovich[1], Aleksey G. Chubarov[1], Svetlana O. Dementyeva[1], and Alexander M. Feigin[1]

[1]A. V. Gaponov-Grekhov Institute of Applied Physics of the Russian Academy of Sciences, 46 Ulyanov Str., 603950 Nizhny Novgorod, Russia

Correspondence to: Mikhail Yu. Kulikov (mikhail_kulikov@mail.ru)

Abstract. The nighttime ozone chemical equilibrium (NOCE) is a key assumption widely employed for various applications in the mesopause region, such as retrieving hard-to-measure characteristics from observations. Previously, the criterion for determining the NOCE boundary was used to analyze its long-term evolution from SABER/TIMED data, primarily at low and middle latitudes. This work focuses on polar latitudes. We demonstrate that the NOCE criterion clearly indicates the main features of the transition zone separating deep and weak O and H diurnal photochemical oscillations. During the polar night, this zone degenerates into a step in their profiles, and the criterion identifies the altitude of this step. Next, we analyze the evolution of the NOCE boundary using SABER/TIMED data in conjunction with MERRA-2 data for the winter–spring period of 2002–2025. We demonstrate that its most pronounced variability is observed at northern latitudes during and after strong SSWs with an elevated stratopause. Prior to or immediately during such warmings, the daily mean boundary can rise to ~87 km. Immediately after, it rapidly descends to 72–74 km and can remain at this altitude for an extended period. Model studies of the winter of 2009 show that the boundary closely follows the variability of the medians of the vertical distributions of O and the volume emission rates of OH*, O*, and O_2*. Thus, we can assume that the NOCE boundary can be used to monitor significant disturbances in both the O_x–HO_x components and the airglows generated by physicochemical processes involving them.

1 Introduction

Ozone is a unique atmospheric trace gas that plays different roles depending on altitude. In particular, stratospheric ozone protects life on our planet by absorbing ultraviolet solar radiation in the wavelength range of 200–315 nm. Moreover, by absorbing radiation in the Herzberg continuum, ozone at these altitudes is the only atmospheric minor gas whose vertical distribution determines the photodissociation rate of the major gas, molecular oxygen. In turn, tropospheric ozone acts as the fourth (in terms of importance) greenhouse gas after H_2O, CO_2 and CH_4. Furthermore, in the boundary layer, ozone is one of the five major pollutants (according to the World Health Organization) that negatively affect the biosphere and human health due to its high toxicity.

In the mesosphere–lower thermosphere (MLT), ozone is involved in reactions between the O_x and

https://doi.org/10.5194/egusphere-2026-4117
Preprint. Discussion started: 15 July 2026

HO_x families ($O+O_3$ and $H+OH+HO_2$), which produce many layered phenomena. Below ~80–87 km, there are "deep" diurnal photochemical oscillations, where the difference between daytime and nighttime values of these components can reach several orders of magnitude due to the diurnal modulation of the photodissociation rates of O_2, H_2O, and O_3. Above ~80–87 km, photochemical oscillations are relatively weak compared to the more pronounced impact of vertical and horizontal transport. As a result, there is a narrow (1–3 km thick) transition region where the regime of photochemical oscillations changes rapidly with height. Above this transition region, O and H concentrations accumulate and reach absolute maxima, forming the corresponding layers, including a layer of stored chemical energy. This leads to the appearance of a secondary ozone maximum and airglow layers of excited OH, O_2 and O observed in the visible and infrared ranges. In particular, the reaction of ozone with atomic hydrogen is the main source of OH airglow, whose intensity spectrum can be used, for example, to derive information about the mesopause temperature. Thus, mesopause photochemistry enables several remote sensing techniques that are widely used for ground-based and satellite monitoring of climate change and wave activity at these altitudes. The chemical heating from exothermic reactions between O_x-HO_x species is one of the major sources of the mesopause energy balance. In particular, this heating can exceed that from turbulent energy dissipation (e.g., Grygalashvyly et al., 2024). Moreover, mesopause photochemistry influences the radiative cooling of this region in the CO_2 15-μm band, is involved in plasma-chemical reactions, and contributes to the formation of ionospheric layers. Note that variations in the O_x-HO_x transition zone height reflect corresponding changes in the O and H layers, and through them, in airglows and other mesopause features. Thus, this characteristic can be considered a sensitive indicator of mesopause processes.

Note also, the mentioned transition of O_x-HO_x behavior with height may occur via the nonlinear response to the diurnal modulation of photodissociation rates, resulting in the appearance of subharmonic (with periods of 2, 3, 4, and more days) or chaotic oscillations of O, O_3, H, OH, and HO_2 (e.g., Sonnemann and Fichtelmann, 1997; Feigin et al., 1998). This unique phenomenon was predicted many years ago (Sonnemann and Fichtelmann, 1987) and further investigated theoretically by taking into account different transport processes (Sonnemann and Feigin, 1999; Sonnemann et al., 1999; Kulikov and Feigin, 2005; Kulikov, 2007; Kulikov et al., 2020), including within the framework of the 3D chemical-transport models (Sonnemann and Grygalashvyly, 2005; Kulikov et al., 2021). The vertical eddy diffusion was revealed as the most important process (Sonnemann and Feigin, 1999; Sonnemann et al., 1999), so that 2-day oscillations can only survive at real diffusion coefficients. At the same time, the eddy diffusion in the zonal direction leads to the appearance of the so-called reaction-diffusion waves in the form of propagating phase fronts of 2-day oscillations (Kulikov and Feigin, 2005; Kulikov et al., 2012; Kulikov et al., 2020). Recently, the first evidence of 2-day photochemical oscillations in the actual mesopause was revealed through the satellite data processing (Kulikov et al., 2021).

At the MLT altitudes, the physicochemical assumptions involving ozone are useful tool for

https://doi.org/10.5194/egusphere-2026-4117
Preprint. Discussion started: 15 July 2026

monitoring poorly measured O_x-HO_x components. In many papers, the rocket and satellite measurements of the ozone and the volume emission rates of OH(v), $O(^1S)$, and $O_2(a^1\Delta_g)$ were applied to retrieve O and H distributions (e.g., Good, 1976; Pendleton et al., 1983; McDade et al., 1985; McDade and Llewellyn, 1988; Evans et al., 1988; Thomas, 1990; Llewellyn et al., 1993; Llewellyn and McDade, 1996; Mlynczak et al., 2007, 2013a, 2013b, 2014, 2018; Smith et al., 2010; Xu et al., 2012; Siskind et al., 2008, 2015). The retrieval approach employs a model of the corresponding airglow and an algebraic equation derived from the assumption of ozone photochemical/chemical equilibrium and relating local O and H values with measurement data. The ternary photochemical equilibrium condition of OH, HO_2, and O_3 produces a useful system of algebraic equations, which was used to retrieve daytime distributions O, H, HO_2, and H_2O from simultaneous O_3 and OH data measured during the satellite CRISTA – MAHRSI campaign (Kulikov et al. 2006, 2009) and to evaluate the quality of simultaneous observations OH, HO_2, and O_3 by MLS/Aura (Kulikov et al. 2018a; Belikovich et al., 2019). Note also that the nighttime ozone chemical equilibrium was used (i) to study hydroxyl emission in the MLT region using simulated and measured data, in particular, OH* mechanisms, morphology and variability caused, for example, by atmospheric tides and gravity wave activity (e.g., Marsh et al., 2006; Nikoukar et al., 2007; Xu et al., 2010, 2012; Kowalewski et al., 2014; Sonnemann et al., 2015); (ii) to analyze the MLT response to sudden stratospheric warmings (SSWs) (e.g., Smith et al., 2009); (iii) to derive exothermic heating rates in the MLT (e.g., Mlynczak et al., 2013b); (iv) to analytically simulate the mesospheric OH* layer response to gravity waves (e.g., Swenson and Gardner, 1998); and (v) to derive the analytical dependence of excited hydroxyl layer number density and peak altitude on atomic oxygen and temperature (e.g., Grygalashvyly et al., 2014; Grygalashvyly, 2015).

The daytime O_3 balance at MLT altitudes is primarily determined by reactions $O+O_2+M \rightarrow O_3+M$, $O_3 + h\nu \rightarrow O_2+O$, $O(^1D)$, and $H+O_3 \rightarrow O_2+OH$ (Kulikov et al., 2017, 2022a). Kulikov et al. (2017) examined O_3 daytime equilibrium within the framework of a 3D chemical-transport model and found it to provide a good approximation everywhere in the MLT region due to the high ozone photodissociation rate. In contrast, nighttime ozone chemical equilibrium (NOCE) is valid above a lower boundary, whose altitude depends on latitude and month. In particular, according to the 3D chemical-transport model, the monthly mean NOCE boundary varies within the range of 81–87 km (Kulikov et al., 2018b). Below this boundary, the local ratio between true O_3 and its equilibrium value may vary widely and reaching several orders of magnitude (e.g., Fig. 5 in Kulikov et al. (2018b)). This means that the error in retrieved data due to the use of the O_3 equilibrium approximation is uncontrollable and may significantly exceed all other errors in the retrieval procedure arising from, for example, uncertainties in measurement data and rate constants. In order to limit the equilibrium approximation error, Kulikov et al. (2018b) developed a robust analytical criterion that allows localizing the boundary of the NOCE using measured or retrieved data. Kulikov et al. (2019) applied this criterion to determine the NOCE boundary using data from the SABER (Sounding of

https://doi.org/10.5194/egusphere-2026-4117
Preprint. Discussion started: 15 July 2026

the Atmosphere using Broadband Emission Radiometry) instrument onboard the TIMED (Thermosphere Ionosphere Mesosphere Energetics and Dynamics) satellite. The space-time distribution of the derived NOCE boundary showed good agreement with model results. Moreover, the application of the NOCE condition below this boundary could lead to a significant (up to 5–8 times) systematic underestimation of the 2-month mean O distribution below 86 km. Recently, Kulikov et al. (2023a) analyzed the long-term evolution of the monthly mean NOCE boundary derived from SABER/TIMED data in 2002–2021. It was revealed that, first, this characteristic at 55°S–55°N contains a clear signal of the 11-year solar cycle and can be considered a sensitive indicator of solar activity. Second, the NOCE criterion at low and middle latitudes reproduces well the altitude and captures the main variations of the transition zone separating deep and weak diurnal oscillations of O and H. In particular, the transition zone at middle latitudes demonstrates a pronounced annual cycle with minimum altitude in winter and maximum altitude in summer. This is a nontrivial effect as summer nighttime H values are substantially higher than those in winter (e.g., Kulikov et al., 2024), which results in shorter ozone lifetimes in summer than in winter. Thus, one would expect an opposite seasonal dependence of the transition zone altitude. Nevertheless, the same results were obtained in model studies by Belikovich et al. (2018) and Kulikov et al. (2018b). In the work by Kulikov et al. (2023a), the discussed effect was explained by the specific nonlinear properties of nighttime mesopause chemistry, which depend strongly on the daytime O/H ratio preceding the night. By design, the NOCE criterion takes into account these properties, ensuring good agreement with the transition zone position. Thus, this criterion is not only a useful technical tool for retrieving unmeasured data from satellite observations, but also a sensitive indicator of O and H layers. As mentioned, many phenomena in the MLT (e.g., airglows) are caused by O and H layers. Thus, one can expect that variations in the main features of these phenomena (e.g., half-width, peak volume emission rates, etc.) are connected with the NOCE boundary position and can be explained/predicted by the NOCE criterion. Finally, Kulikov et al. (2023a) noted abrupt changes in the NOCE boundary at north polar altitudes in winters with powerful SSWs accompanied by elevated (up to ~80–85 km) stratopause events, but a detailed analysis of these variations was outside the scope of that study.

This article focuses on the local evolution of the NOCE boundary at polar latitudes, primarily during winter. The first goal is to study using model data the connection between the NOCE boundary and the spatiotemporal variability of Ox-HOx chemistry at these latitudes; the second is to analyze the evolution of the NOCE boundary from the SABER/TIMED dataset during the winter–spring period, especially before, during, and after SSWs in 2002–2025. In the next section, we present the model data used. In Section 3, we briefly describe the criterion for determining the local altitude of the NOCE boundary and explain the methodology of its application to satellite data. In Section 4, we study how the NOCE boundary is related to the features of O and H oscillations calculated by the 3D model. Section 5 presents the main results obtained from SABER/TIMED data in comparison with zonal wind and temperature in the upper

https://doi.org/10.5194/egusphere-2026-4117
Preprint. Discussion started: 15 July 2026

stratosphere and lower mesosphere from the MERRA-2 reanalysis. Section 6 is devoted to the discussion, followed by concluding remarks.

2 Used data of 3D models

To study the connection between the NOCE boundary at polar latitudes and the transition zone of O_x-HO_x oscillations with altitude, we used our calculations of the NCAR Whole Atmosphere Community Climate Model with thermosphere and ionosphere extension (WACCM-X) (Liu et al., 2018). This is a high- top, interactive 3D chemistry-climate model that describes the global evolution of the atmosphere from the surface to $4.1\cdot10^{-10}$ hPa at 145 pressure-related altitude levels, with a horizontal resolution of 0.95 degrees in latitude and 1.25 degrees in longitude. The vertical resolution of the model at mesopause altitudes is approximately 1.5 km. The integration step is 5 min. The chemical mechanism includes 74 neutrals and 7 ions, 87 photolysis and photoionization processes, 202 gas-phase reactions, and heterogeneous reactions. WACCM-X reproduces many modes of variability and trends in the middle atmosphere, including quasi-biennial oscillations, SSWs, ozone depletion and polar ozone holes, etc.

To study the impact of the SSW during the winter of 2009 on North Polar chemistry and airglow emissions from excited OH*, O*, and O2* states, we used data from an annual run of the Canadian Middle Atmosphere Model (Scinocca et al., 2008) provided by the Canadian Centre for Climate Modelling and Analysis. The pressure, temperature, O, H, O_2, and O_3 profiles allowed us to calculate the distributions of OH(v=1-9), O(^{1}S), and $O_2(b^1\Sigma_g^+)$, according to the airglow models presented by Panka et al. (2021), Gao et al. (2012), and Grygalashvyly et al. (2021), respectively.

3 The NOCE criterion and determination of the NOCE boundary from SABER data

Here, we repeat the theory behind the NOCE criterion following Kulikov et al. (2023b) to improve the readability of this paper, using the same nomenclature as in the original work.

The equilibrium ozone concentration (${O_3}^{eq}$), corresponding to the instantaneous balance between the production and loss terms due to reactions R1 and R2, is given by:

$$ {O_3}^{eq} = \frac{k_1\cdot O\cdot O_2\cdot M}{k_2\cdot H}, \qquad (1)$$

where M is air concentration, and $k_{1,3}$ are the corresponding rate constants of the reactions (see Table 1).

Table 1. List of reactions with corresponding reaction rates (for three-body reactions [cm^6 molecule^{-2} s^{-1}], for two-body reactions [cm^3 molecule^{-1} s^{-1}]) taken from Burkholder et al. (2020).

	Reaction	Rate constant
R1	$O+O_2+M \rightarrow O_3+M$	$k_1 = 6.1\cdot10^{-34}(298/T)^{2.4}$
R2	$H+O_3 \rightarrow O_2+OH$	$k_2 = 1.4\cdot10^{-10}exp(-470/T)$

https://doi.org/10.5194/egusphere-2026-4117
Preprint. Discussion started: 15 July 2026

R3	$O+HO_2 \rightarrow O_2+OH$	$k_3 = 3 \cdot 10^{-11} exp(200/T)$
R4	$H+O_2+M \rightarrow HO_2+M$	$k_4 = 5.3 \cdot 10^{-32} (298/T)^{1.8}$
R5	$H+HO_2 \rightarrow O_2+H_2$	$k_5 = 6.9 \cdot 10^{-12}$
R6	$H+HO_2 \rightarrow O+H_2O$	$k_6 = 1.6 \cdot 10^{-12}$

As mentioned above, the NOCE criterion was suggested in Kulikov et al. (2018b). The main idea is that the local values of O_3 and $O_3{}^{eq}$ are close ($O_3(t) \approx O_3{}^{eq}(t)$), when $\tau_{O_3} \ll \tau_{O_3{}^{eq}}$, where τ_{O_3} is the ozone lifetime and $\tau_{O_3{}^{eq}}$ is the local time scale of $O_3{}^{eq}$:

$$\tau_{O_3} = \frac{1}{k_2 \cdot H}, \tag{2}$$

$$\tau_{O_3{}^{eq}} \equiv \frac{O_3{}^{eq}}{|dO_3{}^{eq}/dt|} = \frac{O}{H \cdot \left|\frac{d}{dt}\left(\frac{O}{H}\right)\right|}\,. \tag{3}$$

Kulikov et al. (2018b) determined the expression for $\tau_{O_3{}^{eq}}$ with the use of a simplified photochemical model describing the O_x-HO_x evolution in the mesopause region (Feigin et al., 1998), so the criterion of the NOCE validity is as follows:

$$Cr = \frac{\tau_{O_3}}{\tau_{O_3{}^{eq}}} = 2\frac{k_1 \cdot k_4 \cdot O_2{}^2 \cdot M^2}{k_2}\left(1 - \frac{k_5+k_6}{k_3}\right) \cdot \frac{1}{k_2 \cdot H \cdot O_3} \ll 1, \tag{4}$$

where k_i are the corresponding reaction constants from Table 1. Calculations with the global 3D chemistry-transport model of the middle atmosphere showed (Kulikov et al. 2018b) that the criterion $\tau_{O_3}/\tau_{O_3{}^{eq}} \leq 0.1$ defines well the boundary of the area where $|O_3/O_3{}^{eq} - 1| \leq 0.1$.

Kulikov et al. (2023b) presented the theory of chemical equilibrium of a certain trace gas n. Strictly mathematically, the cascade of sufficient conditions for $n_i(t) \cong n_i{}^{eq}(t)$ was derived considering its lifetime, equilibrium concentration, and time dependences of these characteristics. In case of the nighttime ozone, it was proved that $\tau_{O_3}/\tau_{O_3{}^{eq}} \ll 1$ is the main condition for NOCE validity and the criterion $\tau_{O_3}/\tau_{O_3{}^{eq}} \leq 0.1$ limits a possible difference between O_3 and $O_3{}^{eq}$ to not more than ~10%. Moreover, Kulikov et al. (2023b) slightly corrected the expression for the criterion (4):

$$\mathrm{Cr} = 2 \cdot \frac{k_1 \cdot O_2 \cdot M}{k_2}\left(k_4 \cdot M \cdot O_2 \cdot \left(1 - \frac{k_5+k_6}{k_3}\right) + k_2 \cdot O_3\right) \cdot \frac{1}{k_2 \cdot H \cdot O_3} \leq 0.1. \tag{5}$$

One more important condition for $O_3 \approx O_3{}^{eq}$ at the time moment t is:

$$e^{\int_{t_{on}}^{t} \tau_{O_3}{}^{-1} dt} \gg 1, \tag{6}$$

where t_{on} is the onset of night. The ozone equilibrium concentration jumps at sunset due to the shutdown of photodissociation. Thus, the condition (6) shows that it takes time for the ozone concentration to reach a new equilibrium. Kulikov et al. (2023b) revealed that, at the solar zenith angle $\chi > 95°$, the condition (6) is fulfilled almost in all cases and the condition (5) becomes the main criterion for NOCE validity. In addition, Kulikov et al. (2023b) demonstrated with the use of a 3-D model that the criterion (5) almost

https://doi.org/10.5194/egusphere-2026-4117
Preprint. Discussion started: 15 July 2026

ideally reproduces the NOCE boundary found by direct comparison of O_3 and ${O_3}^{eq}$ concentrations, see Figure 1 in Kulikov et al. (2023b).

In the paper, we use version 2.0 of the SABER data product (Level2A) for the simultaneously measured profiles of temperature (T), O_3 (at 9.6 μm), and total volume emission rate (VER) of OH* transitions (9→7 and 8→6) at 2.0 μm within the 0.0001–0.02 mbar pressure interval (altitudes approximately 75–105 km) in 2002-2024. Following Kulikov et al. (2023b), we take into account only nighttime data corresponding to the solar zenith angle $\chi > 95°$.

Kulikov et al. (2018a) rewrote the term $k_3 \cdot H \cdot O_3$ in the expression for the NOCE criterion in the form depending on measurable characteristics only with the use of the corresponding OH(v) model by Mlynczak et al. (2013a):

$$k_2 \cdot H \cdot O_3 = VER/A(T,M,O), \tag{7}$$

where $A(T,M,O)$ is the function in square brackets in Eq. (3) in the paper by Mlynczak et al. (2013a) with the parameters corrected by Mlynczak et al. (2018):

$$A(T,M,O) = \frac{0.47\cdot 118.35}{215.05 + 2.5\cdot 10^{-11}\cdot O_2 + 3.36\cdot 10^{-13}\cdot e^{\frac{220}{T}}\cdot N_2 + 3\cdot 10^{-10}\cdot O} + \frac{0.34\cdot 117.21}{178.06 + 4.8\cdot 10^{-13}\cdot O_2 + 7\cdot 10^{-13}\cdot N_2 + 1.5\cdot 10^{-10}\cdot O} +$$

$$\frac{0.47\cdot 117.21\cdot(20.05 + 4.2\cdot 10^{-12}\cdot O_2 + 4\cdot 10^{-13}\cdot N_2)}{(215.05 + 2.5\cdot 10^{-11}\cdot O_2 + 3.36\cdot 10^{-13}\cdot e^{\frac{220}{T}}\cdot N_2 + 3\cdot 10^{-10}\cdot O)\cdot(178.06 + 4.8\cdot 10^{-13}\cdot O_2 + 7\cdot 10^{-13}\cdot N_2 + 1.5\cdot 10^{-10}\cdot O)}. \tag{8}$$

This function is the result of the combination of the equations of physicochemical OH* balance in the v = 8 and v = 9 states, in particular, see Kulikov et al. (2022b) for details. It depends on the constants of the processes describing sources and sinks at the corresponding levels, in particular, the OH(v) removal on collisions with O_2, N_2, and O. Below 86-87 km, $A(T,M,O) \cong A(T,M,O=0) \equiv A(T,M)$ due to relativity small O concentrations. Kulikov et al. (2023a) verified this approximation by direct comparison of $A(T,M)$ and $A(T,M,O)$ and found it to be valid near the NOCE boundary with mean difference between $A(T,M)$ and $A(T,M,O)$ ~ 0.1%. Thus, by combining Eqs. (5) and (7), the NOCE criterion for SABER data can be recast in the following form:

$$VER \geq VER_{min}(T,M) = 20 \cdot \frac{k_1 \cdot O_2 \cdot M}{k_2}\left(k_4 \cdot M \cdot O_2 \cdot \left(1 - \frac{k_5 + k_6}{k_3}\right) + k_2 \cdot O_3\right) \cdot A(T,M). \tag{9}$$

One can see that, VER_{min} decreases rapidly with height due to the strong (~M^4) air-concentration dependence. So, this inequality is well fulfilled at 105 km, but the relationship at 70-75 km is inverse. The local position of the NOCE boundary (geometrical altitude level z_{eq}) is determined according to the criterion (9), where $VER = VER_{min}(T,M)$.

Kulikov et al. (2023b) studied the uncertainty of the retrieved NOCE boundary height. Following the typical analysis presented, for example, in Mlynczak et al. (2013a, 2014), the uncertainty was obtained by calculating the root-sum-square of the individual sensitivity of the retrieved characteristic to the perturbation of O_3, T, rates of reactions, and parameters of the A function. As the result, the uncertainty of the NOCE boundary local height was found to be varied in the range of 0.1-0.3 km.

https://doi.org/10.5194/egusphere-2026-4117
Preprint. Discussion started: 15 July 2026

In this paper, we processed all simultaneous profiles of T, O_3, and VER from 2002 to 2025 and determined the position of the NOCE boundary as a function of time, latitude, and longitude. The latitude range from 82.5°S to 82.5°N was divided into 33 bins 5° each, and all local values of z_{eq} falling into a given bin on a specific day of the year were averaged. Then, we calculated daily mean values of ${z_{eq}}^d$ (hereafter, the superscript *d* denotes the daily average).

4 The connection of the NOCE boundary with spatiotemporal variability of O_x-HO_x chemistry

Figures 1–3 demonstrate the day-to-day evolution of O and H as a function of altitude above various northern polar locations over 3.5 months (from mid-September to December 2017), as simulated by WACCM-X. Thus, Figures 1 and 3 correspond to periods around the autumnal equinox and the winter solstice, respectively. From mid-September to mid-October, pronounced diurnal O and H oscillations occur below 79–80 km, where nighttime values drop by several orders of magnitude relative to daytime values. These oscillations are driven by variations in solar radiation and high nighttime loss rates of HOx and O, which are nonlinearly dependent on air concentration. Above 83–85 km, the behavior of O and H is fundamentally different. First, the diurnal range between minimum and maximum values is significantly reduced. Second, variations on multi-day timescales predominate in the corresponding spectra. The two modes (upper and lower) of O and H behavior are connected vertically by a transition zone several kilometers thick, which is characterized by sharp vertical gradients in the mean daily concentrations of these species. Note that the black lines in Figures 1–3 indicate the NOCE boundary according to criterion (5). An interesting feature is observed in the dynamics of the $\mathrm{Cr} = 0.1$ contour line, which is typical of most nights in Figure 1. Over the course of a single night, this line traverses the transition zone, moving from its lower part, where the lower mode of O and H behavior still persists, to the upper part of the transition zone, where the upper mode is already established. Thus, as at middle and low latitudes (Kulikov et al., 2023a), the NOCE criterion clearly indicates the local position and thickness of the transition zone. The duration of daylight decreases as the year progresses; this manifests relatively weakly in the upper region, but strongly in the lower region. Specifically, below the transition zone (see Figure 2), the mean daily concentrations of O and H decrease noticeably, and their diurnal oscillations become less pronounced or periodically disappear (i.e., they are obscured by variations on other timescales). This is especially noticeable at 82.5°N. Finally, in December (see Figure 3), the mean daily concentrations of O and H at lower altitudes drop to such low levels that the transition zone effectively "degenerates" into a step in the vertical profiles of these species, and the NOCE criterion marks the altitude of this transition. It should be noted that below 75 km, diurnal oscillations remain noticeable, which is likely due to a combined effect of atmospheric dynamics and chemical relaxation.

https://doi.org/10.5194/egusphere-2026-4117
Preprint. Discussion started: 15 July 2026

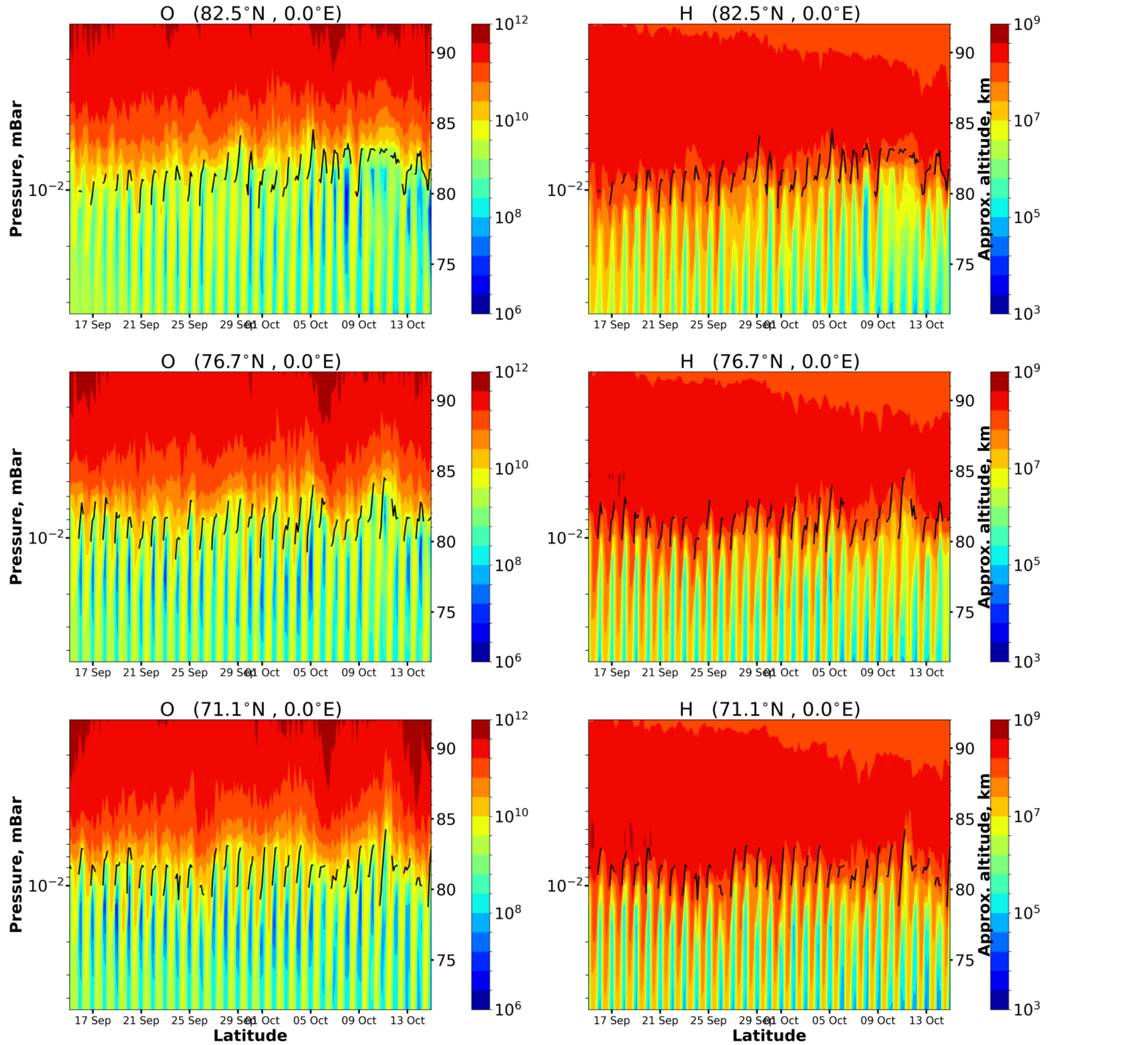

Figure 1. O and H time-height variations above different polar points in September - October 2017 calculated by 3D chemical transport model WACC-X. Black lines point the NOCE boundary altitude in accordance to criterion (5) (Cr = 0.1).

https://doi.org/10.5194/egusphere-2026-4117
Preprint. Discussion started: 15 July 2026

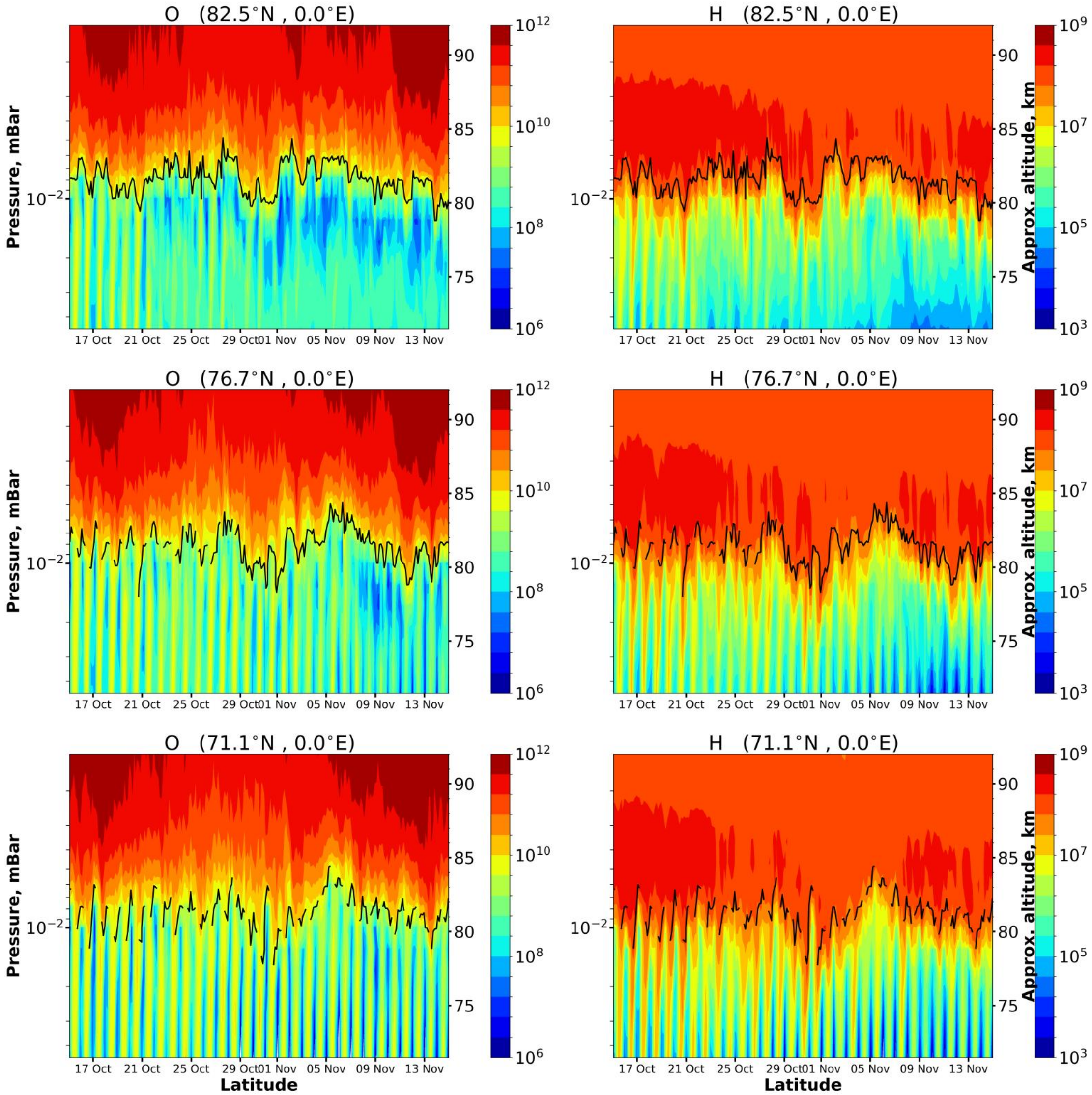

Figure 2. The same as in Fig. 1, but in October - November.

https://doi.org/10.5194/egusphere-2026-4117
Preprint. Discussion started: 15 July 2026

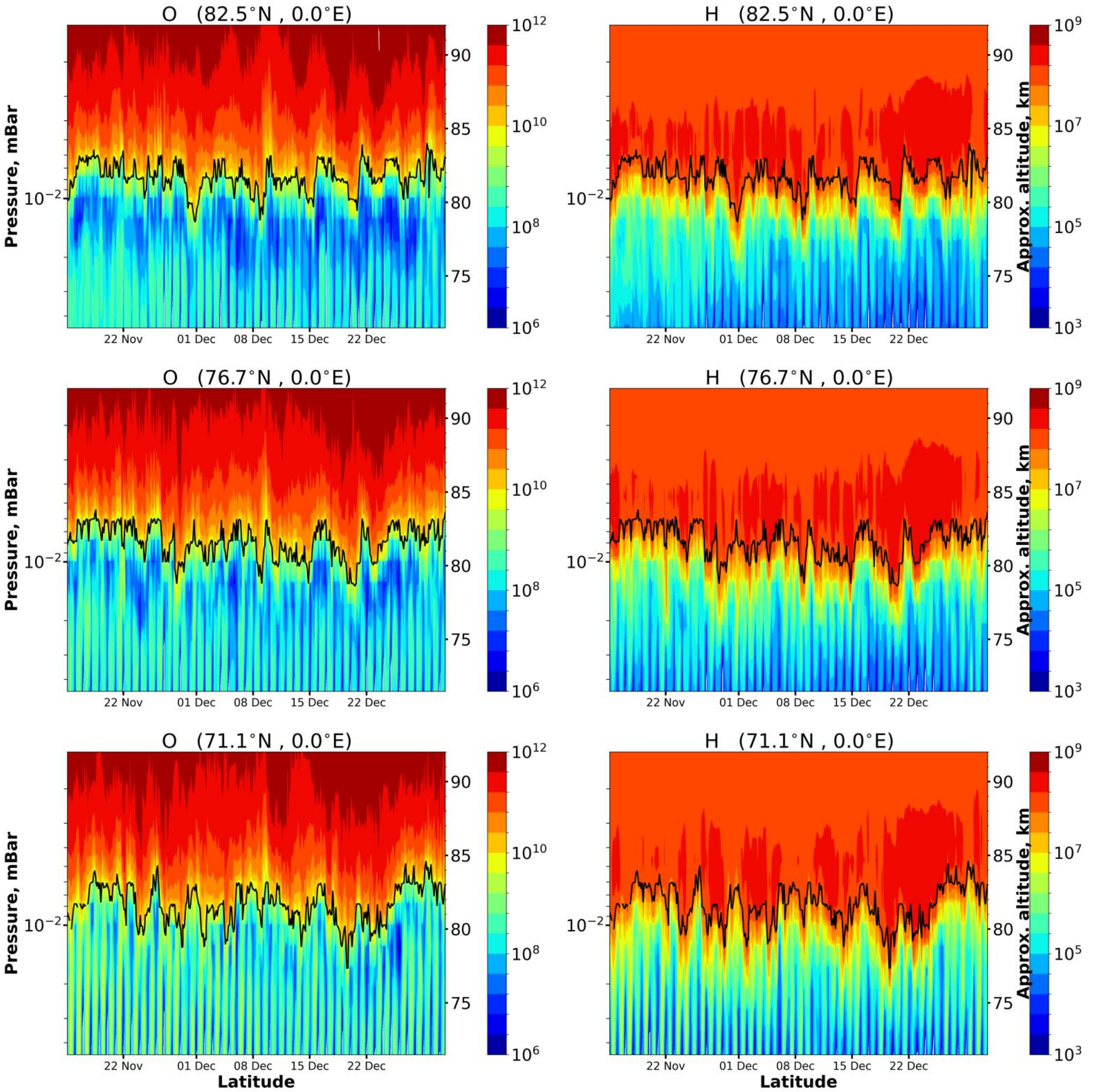

Figure 3. The same as in Fig. 1, but in November - December.

5 NOCE boundary in the polar winters of 2002-2025 from SABER/TIMED data: main results and discussion

Figures 4-5 present contour maps showing the northern latitude–time evolution of ${z_{eq}}^{d}$ from January to March between 2002 and 2025. The strongest disturbances can be seen above 60ºN in early 2004, 2006, 2009, 2012, 2013, and 2019. These winters are known for remarkable major SSWs followed by elevated stratopause (ES) events. In other winters, there were no such strong warming events, but a notable single pulse of ${z_{eq}}^{d}$ may occur (see 2020), when it rose by several kilometers and returned to its original level

https://doi.org/10.5194/egusphere-2026-4117
Preprint. Discussion started: 15 July 2026

within 7-10 days, as well as quasi-periodical oscillations (see 2008) with a characteristic period of ~10-15 days.

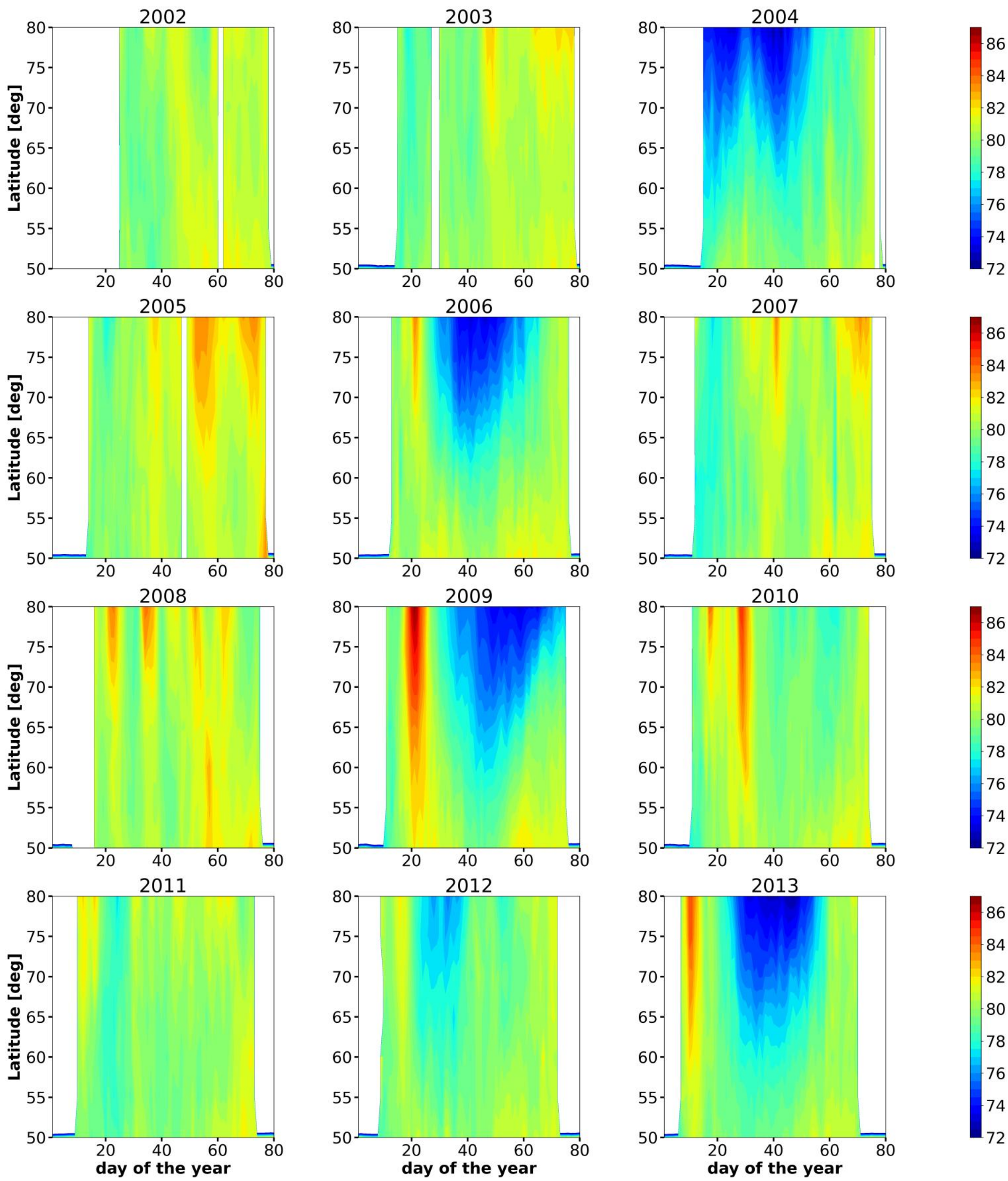

Figure 4. Latitude-time evolution of the daily mean NOCE boundary ${z_{eq}}^{d}$ at northern polar latitudes in different years.

https://doi.org/10.5194/egusphere-2026-4117
Preprint. Discussion started: 15 July 2026

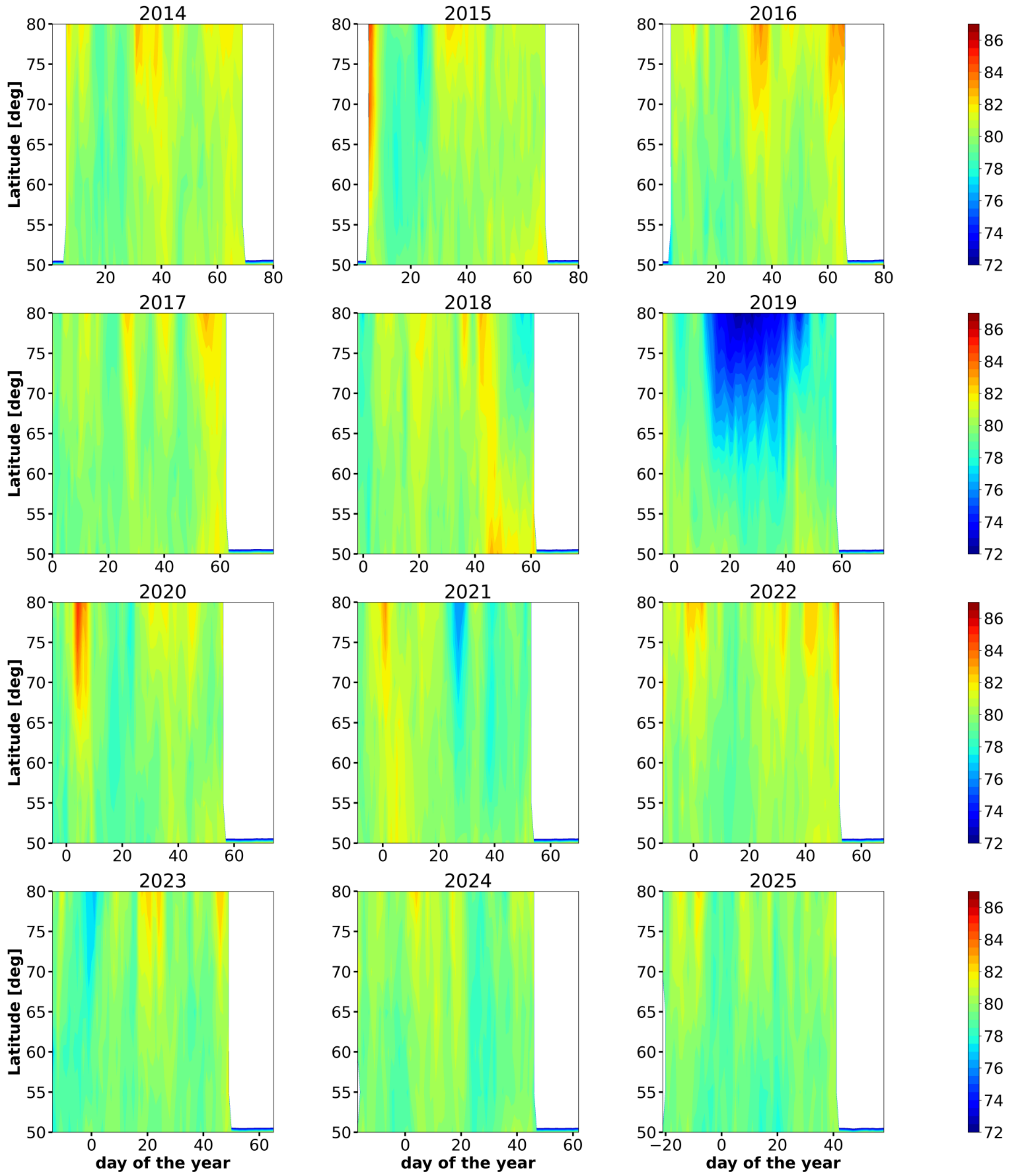

Figure 5. Latitude-time evolution of the daily mean NOCE boundary $z_{eq}{}^{d}$ at northern polar latitudes in different years.

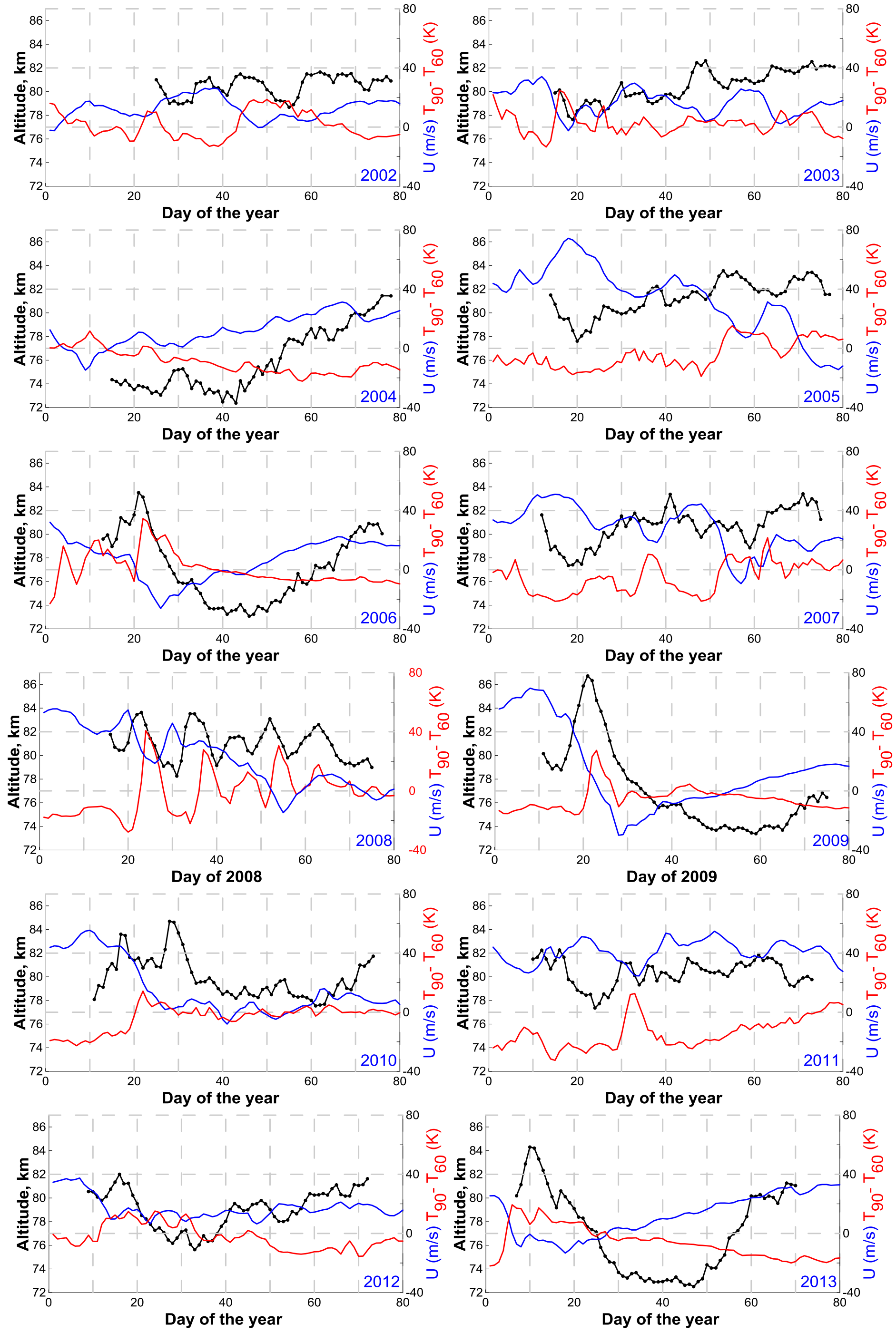

Figure 6. Time evolution of $z_{eq}{}^{d}$ at 80ºN in different years (black lines with dots). The blue lines show the zonal mean wind at 60ºN and 10hPa, the red lines show the temperature difference between the pole and 60ºN at 10hPa.

https://doi.org/10.5194/egusphere-2026-4117
Preprint. Discussion started: 15 July 2026

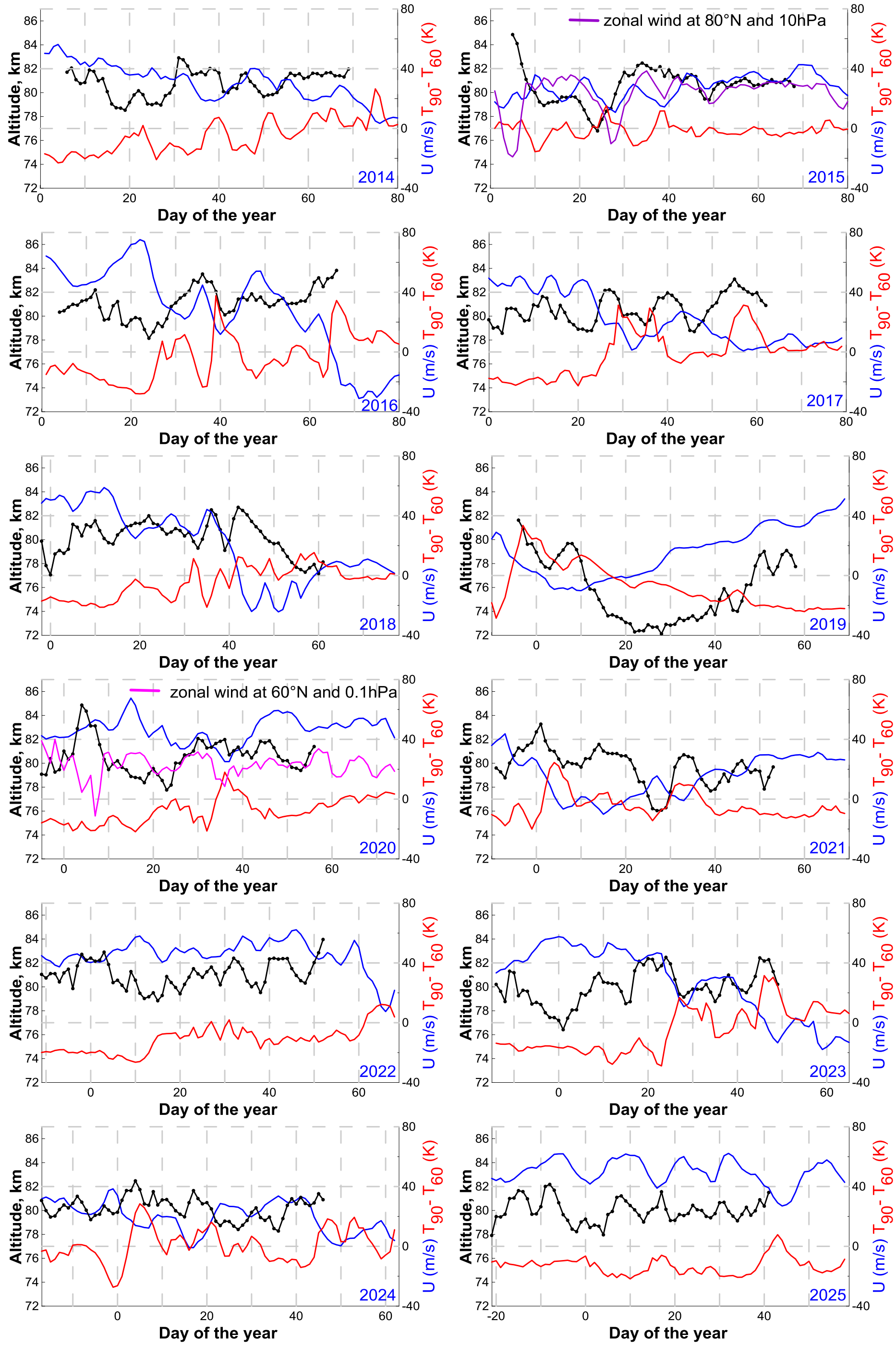

Figure 7. Time evolution of $z_{eq}{}^{d}$ at 80ºN in different years (black lines with dots). The blue lines show the zonal mean wind at 60ºN and 10hPa, the red lines show the temperature difference between the pole and 60ºN at 10hPa.

https://doi.org/10.5194/egusphere-2026-4117
Preprint. Discussion started: 15 July 2026

It is well known that SSWs are caused by the amplification of planetary waves traveling from the lower atmosphere and their interaction with the zonal flow at stratospheric altitudes. Therefore, winter processes at mesopause altitudes should be considered in the context of the simultaneous dynamics of the upper stratosphere and, in some cases, the lower mesosphere. Therefore, in Figures 6-7, the evolution of ${z_{eq}}^{d}$ at 80ºN is shown together with the dynamics of the zonal mean wind at 60ºN and 10hPa ($U_{60ºN,10hPa}$) and the temperature difference ($\Delta T_{90-60ºN,10hPa}$) between the pole and 60ºN at 10hPa, defined as the difference between the average temperatures in the latitudinal ranges of 80-90ºN and 60-70ºN. Both characteristics were calculated using MERRA-2 reanalysis data for the corresponding years.

In the winter of 2001/2002, there were two major SSWs on 29-Dec-01 and 17-Feb-02, respectively. The satellite geometry of SABER measurements above 55°N allowed us to determine ${z_{eq}}^{d}$ only from the end of January, tracking the last major event. During this SSW, we observe weak variations in ${z_{eq}}^{d}$ within the range of 78.5-81.5 km without a clear correlation with $U_{60ºN,10hPa}$ or $\Delta T_{90-60ºN,10hPa}$.

In the 2002/2003 winter, a major SSW occurred on 18 January; however, due to the late start of dataset, it is impossible to see how it manifested at mesopause altitudes. Only a slight oscillation in ${z_{eq}}^{d}$ can be seen in the final stage of this event. Note that in mid-February, there was a strong (nearly to zero) weakening of the zonal wind followed by its recovery, which was accompanied by a noticeable local increase of ${z_{eq}}^{d}$ against the background of a slow seasonal trend.

The winter of 2003/2004 was notable in the 40-year record of meteorological analyses (Manney et al., 2005). A powerful major SSW occurred on January 5, after which the phenomenon of an elevated stratopause was first recorded. Evidently, the pronounced low values of ${z_{eq}}^{d}$ at 80°N (down to ~72.5 km, see Figure 6) from January 15 onwards were caused by this event. Starting in mid-February, ${z_{eq}}^{d}$ began to recover, reaching ~80 km at the end of the dataset.

The winter of 2004/2005 was characterized by a strong polar vortex, and no major SSW was detected before the final stratospheric warming on March 11. However, it can be noted that, unlike the cases of 2001/2002 and 2002/2003, the variations in ${z_{eq}}^{d}$ demonstrated better agreement with the upper stratospheric dynamics. A comparison of the ${z_{eq}}^{d}$ evolution with $U_{60ºN,10hPa}$ shows a good correlation with a coefficient of approximately -0.8. In particular, the absolute minimum in ${z_{eq}}^{d}$ on 20 January corresponded to a zonal wind increase to 70 m/s, whereas two ${z_{eq}}^{d}$ maxima on days ~55 and ~70 could be caused by a local deep minimum and reversal (<0 m/s) of the zonal wind.

In 2005/2006, the central date of the major SSW was January 21, which corresponded to a noticeable rise in ${z_{eq}}^{d}$ from ~79 km to ~83.5 km. The subsequent rapid drop of this characteristic to ~73 km in February and the following rise to 80–81 km in March can be attributed to the appearance and subsequent disappearance of an elevated stratopause. According to Yamazaki et al. (2025), during this SSW, the stratopause jumped from ~30 km to ~80 km around January 25.

In 2006/2007, a major SSW occurred on February 23. However, this event had little impact on the evolution of ${z_{eq}}^d$. More pronounced variations in ${z_{eq}}^d$ can be seen in mid-January (a drop to ~77 km), which can be associated, similarly to 2005, with a local increase in the zonal wind to ~50 m/s.

In 2007/2008, there were four SSW events: three consecutive minor SSWs and one major event occurring on 25 January, 2 February, 16 February, and 23 February, respectively (Wang and Alexander, 2009). During this period, ${z_{eq}}^d$ demonstrated pronounced quasi-periodic oscillations with a period of ~7–10 days in the range of 78–84 km. At least five maxima of the NOCE boundary height can be observed on 23 January, 3 February, 14 February, 21 February, and 3 March. Thus, the first four ${z_{eq}}^d$ maxima can be attributed to the occurrence of SSWs, whereas the last one could be a manifestation of the seasonal restructuring of stratospheric dynamics with oscillations of the mean zonal wind around zero (Wang and Alexander, 2009).

Evidently, the major SSW in early 2009 was one of the most powerful phenomena with an elevated stratopause ever observed. The central date was determined to be January 24, but 3 days prior, ${z_{eq}}^d$ rapidly (over 5–6 days) rose from ~79 km to ~87 km. The subsequent decline of ${z_{eq}}^d$ below 73.5 km is attributed to the elevated stratopause rising from ~20 km to ~82 km (Yamazaki et al., 2025), which jumped to this altitude around January 31. Note that this winter was characterized by the longest-lasting elevated stratopause, so the minimum values of ${z_{eq}}^d$ persisted for ~3 weeks, delaying the recovery.

In 2009/2010, the central date of the major SSW was February 9. That winter, the evolution of ${z_{eq}}^d$ demonstrated two peaks (~83.5 and 84.5 km), one of which approximately corresponded to the major SSW. The elevated stratopause was weakly developed (from ~50 km to ~72 km, Yamazaki et al., 2025) and short-lived, so the NOCE boundary height did not fall below 77.5–78 km.

The winter of 2010/2011 was strong, and only a minor SSW was detected on February 1. Before this event, ${z_{eq}}^d$ dropped from ~82 to ~77 km, possibly due to zonal wind strengthening. As a result, the subsequent minor SSW led to the recovery of the NOCE boundary height to ~82 km.

The winter of 2011/2012 is notable because there was only a minor SSW (January 11), followed by an elevated stratopause. There was a small jump in ${z_{eq}}^d$ from 80 km to 82 km due to this SSW. The subsequent elevated stratopause, rising from ~40 km to ~80 km (Yamazaki et al., 2025), led to a drop in ${z_{eq}}^d$ to ~76 km at the end of January, followed by a quick recovery to ~80 km in mid-February.

The winter of 2012/2013 was characterized by a powerful major SSW (January 7) followed by an elevated stratopause rising from ~35 km to ~80 km (Yamazaki et al., 2025). As in the cases of 2006 and 2009, intense variations in the NOCE boundary height at 80°N can be seen: a rapid rise of this characteristic from ~80 km to ~84.5 km over 3 days, with a subsequent decline below 73 km due to the elevated stratopause. This event persisted for a considerable time, so the minimum values of ${z_{eq}}^d$ lasted for ~2 weeks before recovery.

https://doi.org/10.5194/egusphere-2026-4117
Preprint. Discussion started: 15 July 2026

The winter of 2013/2014 was quite calm with a few minor SSWs that did not greatly disturb either the zonal wind or ${z_{eq}}^d$. Weak variations in ${z_{eq}}^d$ can be seen within the range of 78–82.5 km without a clear correlation with $U_{60ºN,10hPa}$ or $\Delta T_{90-60ºN,10hPa}$.

The winter of 2014/2015 was characterized by an unusual minor SSW in early January with a remarkable impact on atmospheric dynamics close to that of a major SSW (Manney, 2015). During this time, the zonal wind at 10 hPa reversed above 70°N, which lasted for only a few days (see the purple line in the corresponding panel of Figure 7). Nevertheless, a drop in the stratopause was observed, accompanied by warming of the mesopause. Thus, the ${z_{eq}}^d$ maximum (~84.6 km at 80°N) during this period was caused by the SSW. Note that this maximum extended from the pole down to 55–60°N (see Figure 5). The subsequent strengthening of the vortex and its transformation later in January led to mesopause warming and a drop in ${z_{eq}}^d$ below 77 km.

The winter of 2015/2016 was strong and cold (Matthias et al., 2016) with one minor SSW occurring on 8–9 February. Nevertheless, before this SSW, there were pronounced oscillations in $U_{60ºN,10hPa}$ leading to variations in ${z_{eq}}^d$ in the 78–83 km range.

The winter of 2016/2017 was quite calm with a few minor SSWs that did not greatly disturb either the zonal wind or ${z_{eq}}^d$. Weak variations in ${z_{eq}}^d$ can be seen within the range of 78.5–82.5 km without a clear correlation with $U_{60ºN,10hPa}$ or $\Delta T_{90-60ºN,10hPa}$.

In the 2017/2018 winter, there was a strengthening of the stratospheric polar vortex in late December, which apparently resulted in ${z_{eq}}^d$ variations in the 77–82 km range from late December to early January. A major SSW occurred on 12 February 2018. It was accompanied by mesopause warming around 80 km (Yamazaki et al., 2025), resulting in a decline in ${z_{eq}}^d$ from ~83 km to ~77 km until the end of February.

In the 2018/2019 winter, a powerful major SSW with a subsequent elevated stratopause occurred on January 1, but there was a remarkable gap between the times of polar temperature warming and zonal wind reversal. This is likely the reason why we did not observe a strong ${z_{eq}}^d$ rise, as in the previous cases of 2005/2006, 2008/2009, and 2012/2013. On January 9, the stratopause jumped from ~35 to ~80 km (Yamazaki et al., 2025), warming the mesopause and causing ${z_{eq}}^d$ to fall to ~72 km.

The winter of 2019/2020 was characterized by a remarkably strong stratospheric polar vortex due to unusually weak tropospheric wave activity and wave reflection in the polar upper stratosphere (Lawrence et al., 2020; Lukianova et al., 2021). During the first decade of January 2020, a latitude-altitude splitting of the polar vortex occurred, accompanied by periodic accelerations in the zonal wind, causing a drop and warming of the stratopause, zonal wind disturbances at mesospheric altitudes (see Figure 7 for 2020), and mesopause cooling with temperature inversion layer formation. This was not a typical SSW caused by planetary wave breaking. The subsequent strengthening of the vortex and its transformation later in

https://doi.org/10.5194/egusphere-2026-4117
Preprint. Discussion started: 15 July 2026

January led to mesopause warming and the disappearance of the inversion. Thus, the pronounced pulse-like variation in ${z_{eq}}^{d}$ is a manifestation of the polar vortex's own dynamics, rather than classical warming due to the breakdown of planetary waves from the troposphere.

In the 2020/2021 winter, a powerful major SSW occurred on January 4, which corresponded to a noticeable rise in ${z_{eq}}^{d}$ from 79–79.5 km to ~83.5 km and its subsequent return. At the end of January and the beginning of February, two moderate stratopause elevations were observed, from ~54 to ~75 km and from ~55 to ~70 km (Yamazaki et al., 2025), which caused two local oscillations in ${z_{eq}}^{d}$ with a drop to ~76 km.

The winter of 2021/2022 was quite calm with a stable polar vortex from December to February, leading to weak variations in ${z_{eq}}^{d}$ in the 79–83 km range.

The winter of 2022/2023 was characterized by a strong polar vortex from December to the first half of January, whose strengthening resulted in a drop in ${z_{eq}}^{d}$ from ~81.5 km to ~76 km on January 1. Subsequent variations in ${z_{eq}}^{d}$ were determined by minor and major SSWs in the second half of January and mid-February, respectively.

There were a few minor SSWs in the winter of 2023/2024, which did not greatly disturb ${z_{eq}}^{d}$. One can see weak variations ${z_{eq}}^{d}$ within the range of 78-82 km without a clear correlation with $U_{60ºN,10hPa}$ or $\Delta T_{90-60ºN,10hPa}$.

There were a few minor SSWs in the winter of 2023/2024, which did not greatly disturb ${z_{eq}}^{d}$. Weak variations in ${z_{eq}}^{d}$ can be seen within the range of 78–82 km without a clear correlation with $U_{60ºN,10hPa}$ or $\Delta T_{90-60ºN,10hPa}$.

The winter of 2024/2025 was quite calm with a stable polar vortex from December to February, leading to weak variations in ${z_{eq}}^{d}$ in the 78–82.5 km range.

Figures 8–9 present contour maps showing the southern latitude–time evolution of ${z_{eq}}^{d}$ from June to September between 2002 and 2025. Compared to the Northern Hemisphere maps in Figures 4–5, significantly weaker ${z_{eq}}^{d}$ variations can be seen. The strongest disturbances was above 60°S during the winters of 2002, 2004, 2012, 2014, 2017, and 2023. It is well known that southern SSWs are much rarer than northern ones. A major SSW occurred in 2002, which essentially influenced the Antarctic ozone hole that year. The SSW of 2019 was minor but exhibited the largest temperature variations ever recorded in the southern winter polar stratosphere. The winter of 2024 was characterized by two successive minor SSWs in mid-July and early August. Vincent et al. (2025) identified all southern SSWs between 1998 and 2019 using MERRA-2 data. However, most central dates fall outside the time interval where the satellite geometry of SABER allows us to determine ${z_{eq}}^{d}$ above 55°S. Figures 10–11 present the time evolution of ${z_{eq}}^{d}$ at 80ºS together with $U_{60ºS,10hPa}$ and $\Delta T_{90\text{-}60ºS,10hPa}$. In addition, we included the temperature at the 0.1

https://doi.org/10.5194/egusphere-2026-4117
Preprint. Discussion started: 15 July 2026

hPa ($T_{60ºS,0.1hPa}$), calculated using MERRA-2 reanalysis data, as an indicator of lower mesosphere dynamics, and compared its time evolution with that of ${z_{eq}}^{d}$.

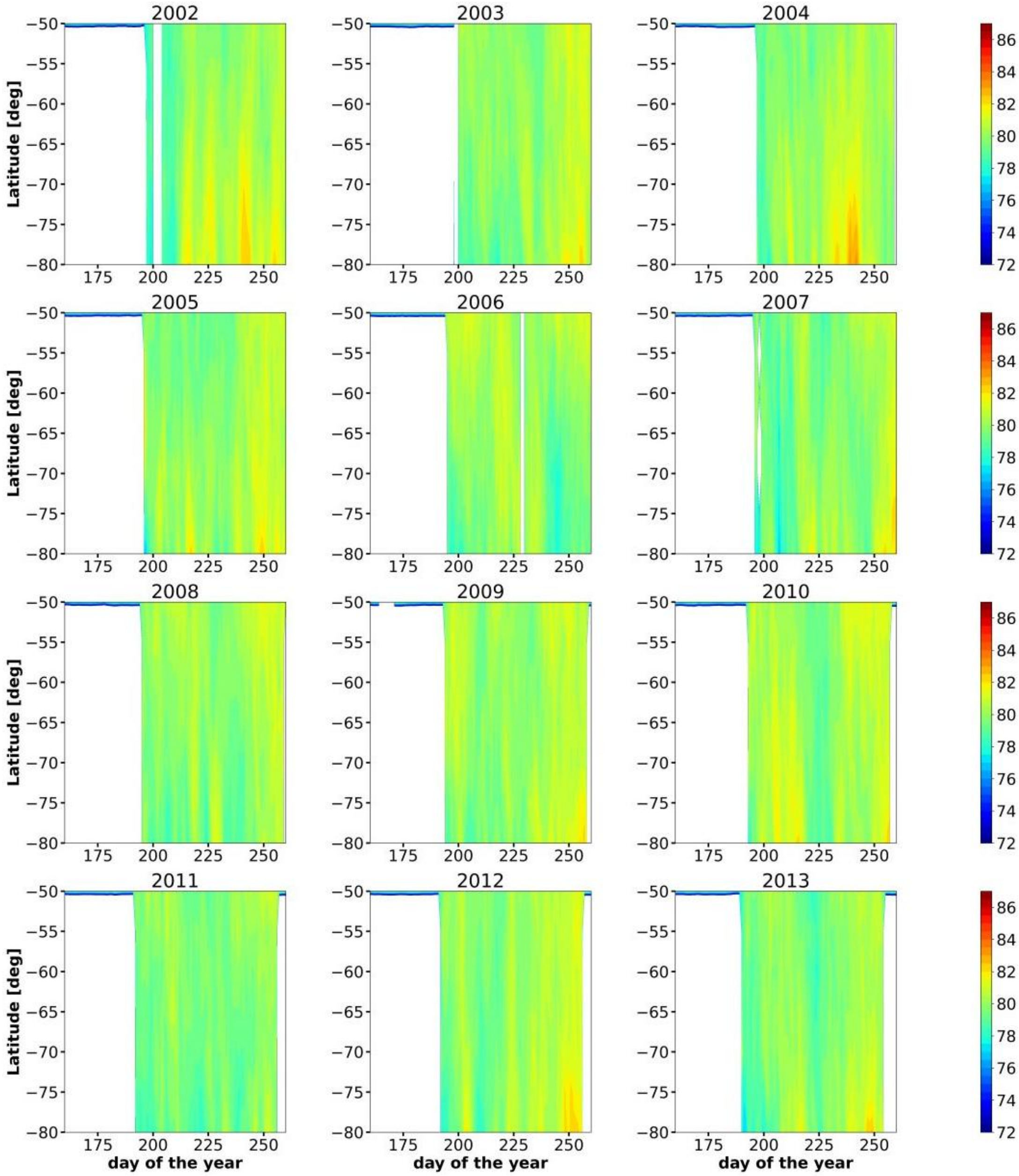

Figure 8. Latitude-time evolution of the daily mean NOCE boundary ${z_{eq}}^{d}$ at southern polar latitudes in different years.

https://doi.org/10.5194/egusphere-2026-4117
Preprint. Discussion started: 15 July 2026

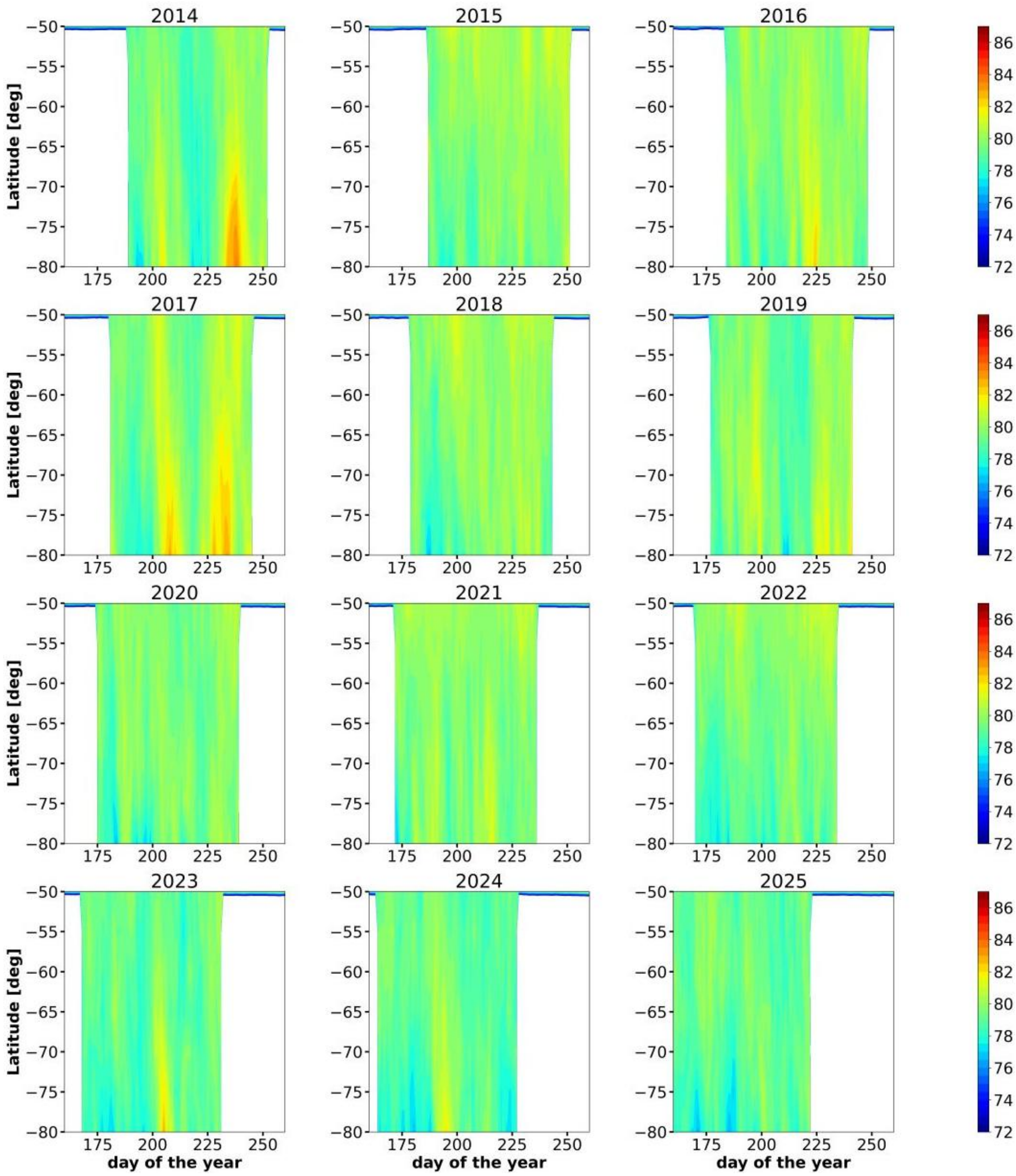

Figure 9. Latitude-time evolution of the daily mean NOCE boundary $z_{eq}{}^{d}$ at southern polar latitudes in different years.

https://doi.org/10.5194/egusphere-2026-4117
Preprint. Discussion started: 15 July 2026

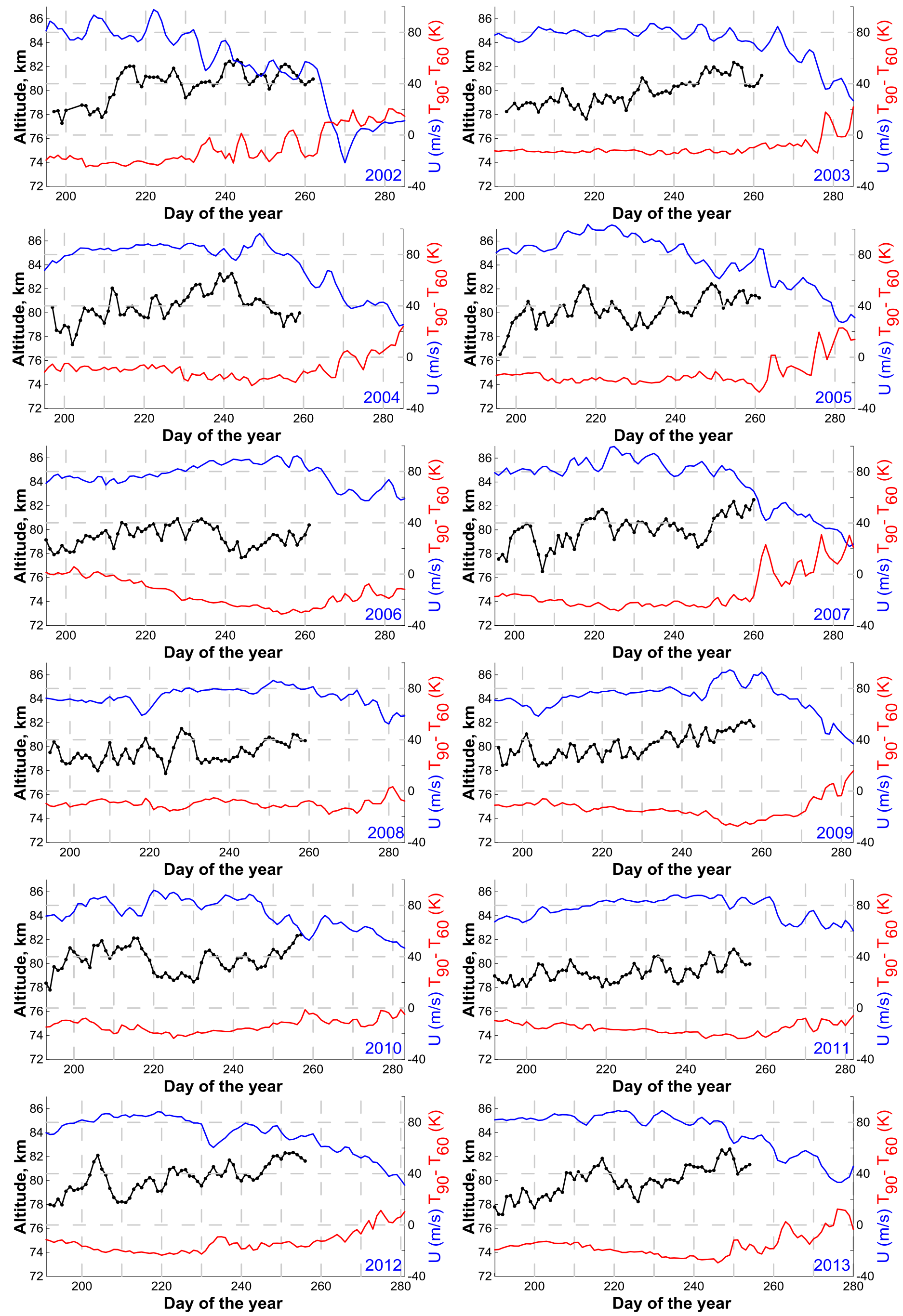

Figure 10. Time evolution of $z_{eq}{}^{d}$ at 80ºS in different years (black lines with dots). The blue lines show the zonal mean wind at 60ºS and 10hPa, the red lines show the temperature difference between the pole and 60ºS at 10hPa.

https://doi.org/10.5194/egusphere-2026-4117
Preprint. Discussion started: 15 July 2026

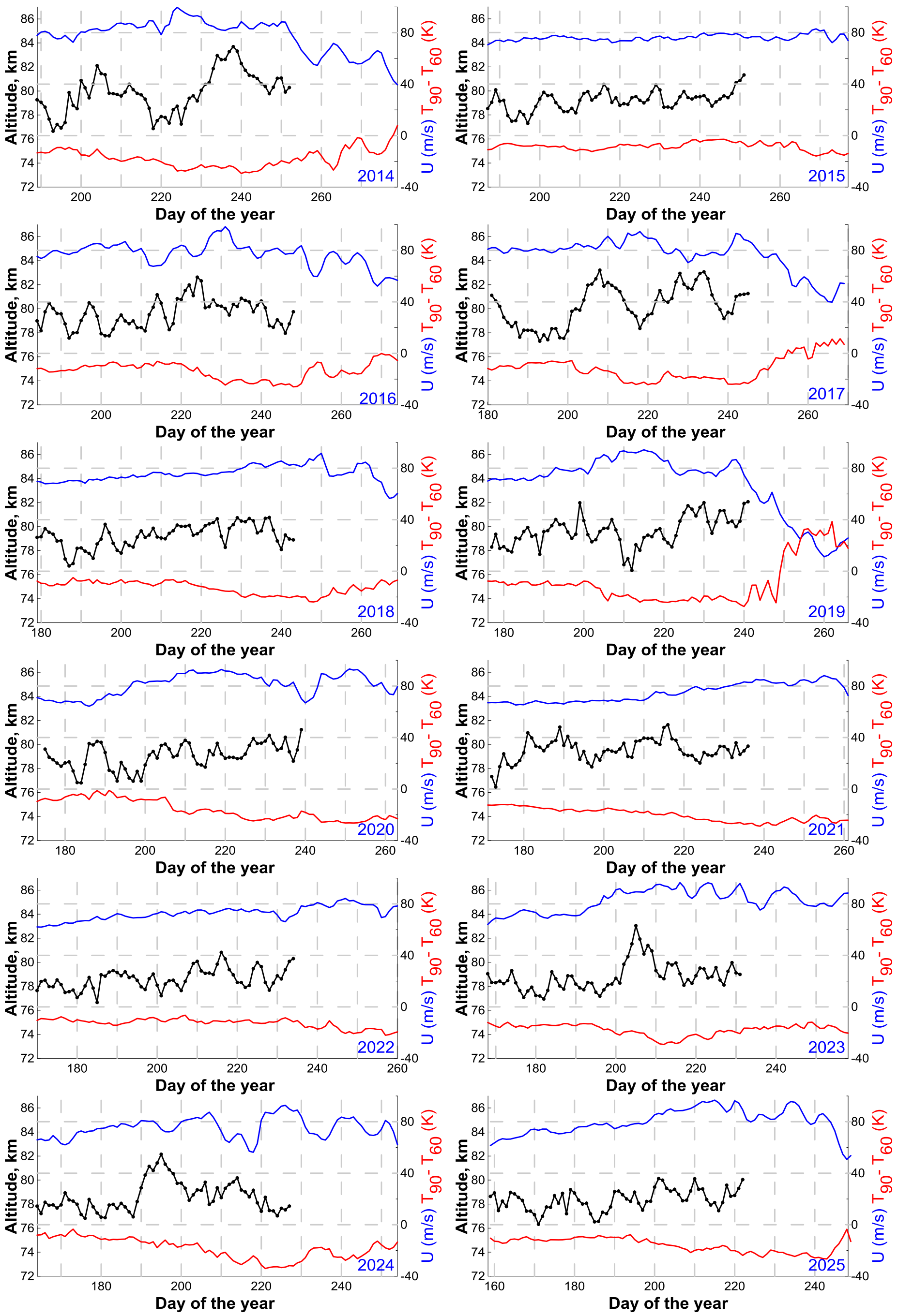

Figure 11. Time evolution of $z_{eq}{}^{d}$ at 80ºS in different years (black lines with dots). The blue lines show the zonal mean wind at 60ºS and 10hPa, the red lines show the temperature difference between the pole and 60ºS at 10hPa.

https://doi.org/10.5194/egusphere-2026-4117
Preprint. Discussion started: 15 July 2026

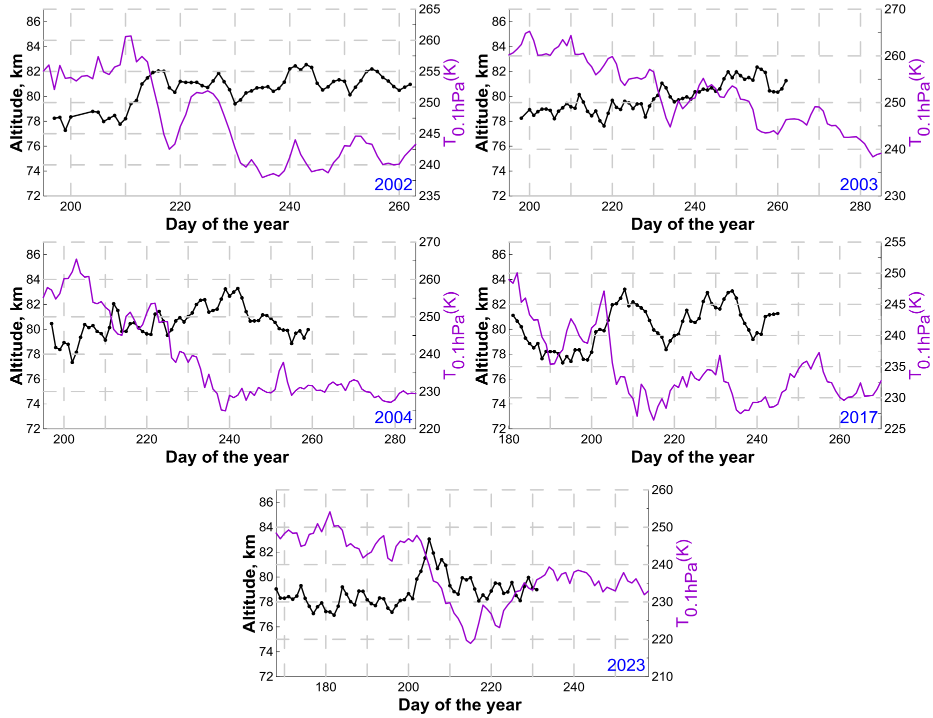

Figure 12. Time evolution of $z_{eq}{}^{d}$ at 80ºS (black lines with dots) versus the temperature at 60ºS and 0.1hPa in the selected years.

The presented time evolution of $z_{eq}{}^{d}$ at 80°S can be classified into one of four types: (1) monotonic growth, as in 2003, 2009, 2011, 2015, or 2022; (2) a step-like change, as in 2002, or a slope break, as in 2004; (3) an impulse-like disturbance, as in 2012, 2023, or 2024; (4) quasi-periodic oscillations with a period of ~20–30 days, as in 2014 or 2017. According to Vincent et al. (2025), the central dates of the minor SSWs in 2002–2019 captured by SABER measurements were 23 August 2002 (day 235 of the year), 2 September 2002 (day 245), 13 September 2002 (day 256), 6 August 2008 (day 218), 2 August 2010 (day 214), 20 August 2012 (day 233), and 7 September 2013 (day 250). Only a minor manifestation of these events can be seen in the evolution of $z_{eq}{}^{d}$ in Figures 10–11. According to Zi et al. (2025), the central dates of two minor SSWs in 2024 were 13 July 2024 (day 195 of the year) and 4 August 2024 (day 217). It can be seen from Figure 11 that the first event corresponded to a local $z_{eq}{}^{d}$ rise from ~77 km to ~82 km, but the second one did not significantly disturb $z_{eq}{}^{d}$. A comparison with the temperature at 0.1 hPa (see Figure 12) shows that many features of the $z_{eq}{}^{d}$ evolution can be explained by the dynamics of the polar vortex in the lower mesosphere. In particular, the step in $z_{eq}{}^{d}$ in 2002 and the impulse in 2023 were accompanied by similar behavior of $T_{60ºS,0.1hPa}$; the monotonic growth of $z_{eq}{}^{d}$ in 2003 corresponded to gradual cooling of the lower mesosphere; the slope break in 2004 showed a strong anticorrelation (with a

https://doi.org/10.5194/egusphere-2026-4117
Preprint. Discussion started: 15 July 2026

coefficient of ~ -0.8) with $T_{60ºS,0.1hPa}$; and the temperature of the lower mesosphere in 2017 also exhibited quasi-periodic oscillations with a period close to that of the $z_{eq}{}^{d}$ oscillations.

6 Discussion

The sharp change in the diurnal oscillations of O and H above 80 km in Figure 1 is caused by the altitude dependence of the reaction rates that determine the chemical lifetimes of these components. The main loss processes for O at these altitudes are the reactions $O + OH \rightarrow O_2 + H$ and $O + HO_2 \rightarrow O_2 + OH$, whereas the main loss processes for H are the reactions $H+HO_2 \rightarrow O_2+H_2$ и $H+HO_2 \rightarrow O+H_2O$ (Kulikov et al., 2023b). Kulikov et al. (2023a), based on the equations describing purely chemical O and H nighttime evolution, evaluated the nighttime lifetimes of O and H:

$$\tau_O \equiv \frac{O}{|dO/dt|} = \frac{1}{2\cdot k_4\cdot M\cdot O_2}\cdot\left(\frac{O}{H}\right)_{t=t_0} - \left(1-\frac{k_5+k_6}{k_3}\right)\cdot(t-t_0), \quad (9)$$

$$\tau_H \equiv \frac{H}{|dH/dt|} = \frac{1}{2\cdot k_4\cdot M\cdot O_2}\cdot\frac{k_3}{k_5+k_6}\cdot\left(\frac{O}{H}\right)_{t=t_0} - \left(\frac{k_3}{k_5+k_6}-1\right)\cdot(t-t_0), \quad (10)$$

where t is the local time, t_0 is the onset of night, $\left(\frac{O}{H}\right)_{t=t_0}$ is the O/H ratio at the onset of night. Note that $k_3 \gg k_5 + k_6$ (see Table 1). Above the NOCE boundary: $O_3 \approx O_3{}^{eq} = \frac{k_1\cdot O\cdot O_2\cdot M}{k_2\cdot H}$, then $\left(\frac{O}{H}\right)_{t=t_0} = \frac{(O_3)_{t=t_0}}{M^2}$. Moreover, in the transition zone, relative concentration of ozone (O_3/M) begins to increase, forming a secondary maximum at 90-95 km. This means that the first terms in equations (9-10) increase with altitude faster than $\frac{1}{M^3}$, leading to approximately the same altitude dependence for τ_O and τ_H. Thus, the lower mode of O and H evolution, characterized by deep diurnal oscillations, corresponds to the condition $\tau_{O,H} \ll T_n$, where T_n is duration of the night, whereas the weak diurnal oscillations of O and H at higher altitudes correspond to the opposite condition: $\tau_{O,H} \gg T_n$. Consequently, the existence of a narrow transition zone connecting the two modes of O and H oscillations is due to a sharp increase in their lifetimes with increasing altitude.

In the ozone equilibrium approximation, criterion (5) can be rewritten as follows:

$$\mathrm{Cr} = 2\cdot\left(k_4\cdot M\cdot O_2\cdot\left(1-\frac{k_5+k_6}{k_3}\right)+k_2\cdot O_3\right)\cdot\frac{1}{k_2\cdot O} \leq 0.1. \quad (11)$$

It can be seen that the Cr=0.1 contour corresponds to the following expression:

$$k_2\cdot O = 20\cdot\left(k_4\cdot M\cdot O_2\cdot\left(1-\frac{k_5+k_6}{k_3}\right)+k_2\cdot O_3\right), \quad (12)$$

which imposes strong constraints on the O concentration at the NOCE boundary. Note that the product $k_4\cdot M\cdot O_2$ is the dominant term of this relation, which also determines the lifetimes of O and H in (9-10). As can be seen from Figure 1, at the beginning of the night, the NOCE boundary lies in the region exhibiting deep diurnal O oscillations. However, since the O concentration at these altitudes drops by 1–2 orders of magnitude or more during the night, the NOCE boundary, according to Equation (12), must

https://doi.org/10.5194/egusphere-2026-4117
Preprint. Discussion started: 15 July 2026

inevitably rise to those altitudes where a high O concentration persists at the end of the night, i.e., in the region of weak diurnal variations of this component. This is why, during each night, the $\mathrm{Cr} = 0.1$ contour cuts through the transition zone, passing from its lower part to the upper one, and clearly captures its main features (local position and thickness).

The analysis presented in Section 5 shows that the most pronounced variability of the NOCE boundary at north polar latitudes occurs during and after strong SSWs with subsequent elevated stratopause events. Just prior to or directly during such warming, the daily mean boundary near the North Pole can jump to 87 km, and local values may be even higher, up to 90-92 km. This means that during these periods, methods for retrieving poorly measured mesopause characteristics (in particular, O), based on the ozone equilibrium condition, may yield significant uncontrolled errors below these altitudes due to the breakdown of this equilibrium. At the same time, immediately after such SSWs, the NOCE boundary rapidly drops down up to 72-74 km and can remain there for a long time.

Thus, during an elevated stratopause event, the altitude range over which the ozone equilibrium condition is well satisfied is significantly expanded and can be used for retrieving O and other characteristics well below 80 km. Furthermore, according to Equation (12), such strong variations (first upward, then downward) of the NOCE boundary during such SSWs should reflect specific features of the dynamics of the vertical profile of O and the airglow emissions caused by O_x-HO_x chemistry. Figure 13 presents the evolution of these characteristics in January–February 2009 at ~80°N, simulated using data from the Canadian Middle Atmosphere Model. It can be seen that the NOCE boundary closely follows the variability of the median vertical distributions of O and the volume emission rates of OH(v=1-9), O(^{1}S), and $O_2(b^1\Sigma_g^+)$. Thus, we can assume that the boundary can be used to monitor significant disturbances in both the O_x–HO_x components and the airglows generated by physicochemical processes involving them.

https://doi.org/10.5194/egusphere-2026-4117
Preprint. Discussion started: 15 July 2026

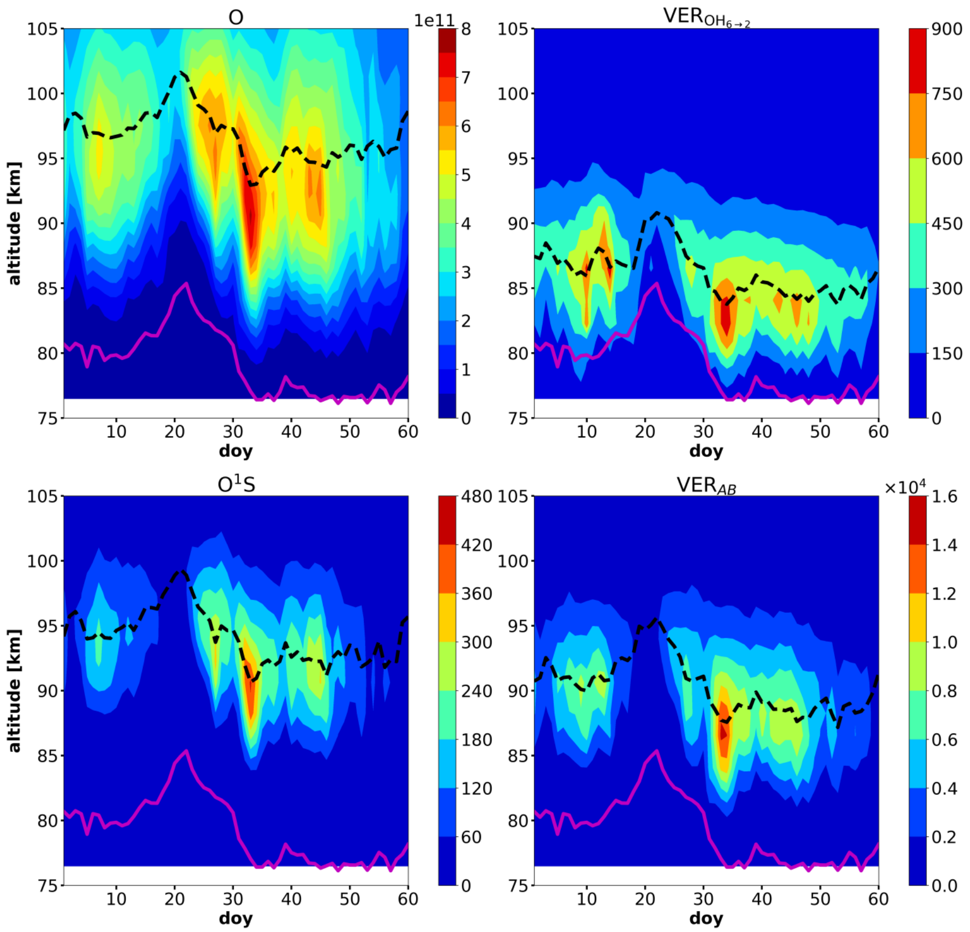

Figure 13. Time evolution of vertical distributions of O and the volume emission rates of OH(6-2), O(^{1}S) at 557.7 nm, and $O_2(b^1\Sigma_g^+)$ at 762 nm (Atmospheric Band) at ~80°N in January–February 2009, simulated using data from the Canadian Middle Atmosphere Model. The black dotted lines show the medians of the presented vertical distributions, magenta line shows the NOCE boundary.

7 Conclusions

As at mid- and low latitudes, the NOCE criterion clearly indicates the local position and thickness of the transition zone separating deep and weak photochemical oscillations of O and H caused by the diurnal variations in solar radiation. This is due to the strong dependence of the NOCE boundary position on the altitude of the layer characterized by a relatively high O concentration. During the polar night, the transition zone effectively "degenerates" into a step in the vertical profiles of these components, and the NOCE criterion identifies the altitude of this step.

The most pronounced variability of the NOCE boundary at northern polar latitudes is observed during and after strong SSWs with subsequent stratopause elevation events. Just prior to or directly during

https://doi.org/10.5194/egusphere-2026-4117
Preprint. Discussion started: 15 July 2026

such warmings, the daily mean altitude of the boundary near the North Pole can jump to 87 km, while local values can be even higher, up to 90–92 km. Immediately after such SSWs, the NOCE boundary rapidly descends to 72–74 km and can remain there for a long time. Thus, the altitude range where the ozone equilibrium condition is valid to determining O and other mesopause characteristics changes significantly during such events. Model studies of 2009 winter show the NOCE boundary well repeat the variability of the medians of the vertical distributions O and volume emission rates of OH(v=1-9), O(^{1}S), and $O_2(b^1\Sigma_g^+)$.

At southern polar latitudes, variations in the NOCE boundary values during winter are significantly weaker than at northern latitudes. These variations are generally unrelated to minor SSWs during these years, but can be explained by the dynamics of the polar vortex in the lower mesosphere.

Data availability. The SABER data are obtained from the website (https://saber.gats-inc.com), last access: 1 July 2026, Mlynczak et al. (2018). CMAM data are obtained from https://climate-modelling.canada.ca/climatemodeldata/cmam/, last access: 1 July 2026, Scinocca et al. (2008). The MERRA-2 data are available publicly from the MERRA-2 website: https://gmao.gsfc.nasa.gov/reanalysis/MERRA-2/, last access: 1 July 2026, Gelaro et al., 2017).

Code availability. As a component of the community earth system model, WACCM-X source code are publicly available at http://www.cesm.ucar.edu), last access: 1 July 2026, Liu et al. (2018).

Author contributions. MK and MB performed data processing and analysis and wrote the manuscript. AC, SD, and AM contributed to reviewing the article.

Competing interests. The authors declare that they have no conflict of interest.

Acknowledgements. The authors are grateful to the SABER team for data availability.

Financial support.

References

Belikovich, M. V., Kulikov, M. Yu, Grygalashvyly, M., Sonnemann, G. R., Ermakova, T. S., Nechaev, A. A., and Feigin, A. M.: Ozone chemical equilibrium in the extended mesopause under the nighttime conditions, Adv. Space Res., 61, 426–432, https://doi.org/10.1016/j.asr.2017.10.010, 2018.

Belikovich MV, Kulikov MYu, Nechaev AA, Feigin AM (2019) Evaluation of the atmospheric minor species measurements: a priori statistical constraints based on photochemical modeling. Radiophys Quantum El 61:1–15. https:// doi. org/ 10. 1007/ s11141- 019- 09918-5

Burkholder, J. B., Sander, S. P., Abbatt, J., Barker, J. R., Cappa, C., Crounse, J. D., Dibble, T. S., Huie, R. E., Kolb, C. E., Kurylo, M. J., Orkin, V. L., Percival, C. J., Wilmouth, D. M., and Wine, P. H.: Chemical Kinetics and Photochemical Data for Use in Atmospheric Studies, Evaluation No. 19, JPL Publication 19-5, Jet Propulsion Laboratory, Pasadena, http://jpldataeval.jpl.nasa.gov, 2020.

Evans, W. F. J., McDade, I. C., Yuen, J., and Llewellyn, E. J.: A rocket measurement of the O_2 infrared atmospheric (0-0) band emission in the dayglow and a determination of the mesospheric ozone and atomic oxygen densities, Can. J. Phys., 66, 941–946, https://doi.org/10.1139/p88-151. 1988.

Gao, H., Nee, J.-B., Xu, J.: The emission of oxygen green line and density of O atom determined by using ISUAL and SABER measurements, Ann. Geophys., 30, 695–701, https://doi.org/10.5194/angeo-30-695-2012, 2012.

Gelaro, R., McCarty, W., Suárez, M. J., Todling, R., Molod, A., Takacs, L., Randles, C. A., Darmenov, A., Bosilovich, M. G., Reichle, R., Wargan, K., Coy, L., Cullather, R., Draper, C., Akella, S., Buchard, V., Conaty, A., da Silva, A. M., Gu, W., Kim, G.-K., Koster, R., Lucchesi, R., Merkova, D., Nielsen, J. E., Partyka, G., Pawson, S., Putman, W., Rienecker, M., Schubert, S. D., Sienkiewicz, M., and Zhao, B.: The modern-era retrospective analysis for research and applications, version 2 (MERRA-2), J. Climate, 30, 5419–5454, https://doi.org/10.1175/JCLI-D-16-0758.1, 2017.

Good, R. E.: Determination of atomic oxygen density from rocket borne measurements of hydroxyl airglow, Planet. Space Sci., 24, 389–395, https://doi.org/10.1016/0032-0633(76)90052-0, 1976.

Grygalashvyly, M., Sonnemann, G. R., Lübken, F.-J., Hartogh, P., and Berger, U.: Hydroxyl layer: Mean state and trends at midlatitudes, J. Geophys. Res. Atmos., 119, 12,391–12,419, https://doi.org/10.1002/2014JD022094, 2014.

Grygalashvyly, M.: Several notes on the OH* layer, Ann. Geophys., 33, 923-930, https://doi.org/10.5194/angeo-33-923-2015, 2015.

Grygalashvyly, M., Strelnikov, B., Eberhart, M., Hedin, J., Khaplanov, M., Gumbel, J., Rapp, M., Lübken, F.-J., Löhle, S., and Fasoulas, S.: Nighttime $O(^1D)$ and corresponding Atmospheric Band emission (762 nm) derived from rocket-borne experiment, J. Atmos. Sol.-Terr. Phys., 213, 105522, https://doi.org/10.1016/j.jastp.2020.105522, 2021.

Grygalashvyly, M., Strelnikov, B., Strelnikova, I., Rapp, M., Lübken, F.-J., Schütt, C., Stephan, C., Eberhart, M., Löhle, S., and Fasoulas S.:.Chemical heat derived from rocket-borne WADIS-2 experiment, Earth Planets Space, 76, 180, https://doi.org/10.1186/s40623-024-02129-x, 2024.

Feigin, A. M., Konovalov, I. B., and Molkov, Y. I.: Towards understanding nonlinear nature of atmospheric photochemistry: Essential dynamic model of the mesospheric photochemical system., J. Geophys. Res.: Atmos., 103, 25,447–25,460, https://doi.org/10.1029/98JD01569, 1998.

Konovalov, I. B., and Feigin, A. M.: Towards an understanding of the non-linear nature of atmospheric photochemistry: origin of the complicated dynamic behavior of the mesospheric photochemical system,

https://doi.org/10.5194/egusphere-2026-4117
Preprint. Discussion started: 15 July 2026

Nonlin. Processes Geophys., 87-104, https://doi.org/10.5194/npg-7-87-2000, 2000.

Kowalewski, S., v. Savigny, C., Palm, M., McDade, I. C., and Notholt, J.: On the impact of the temporal variability of the collisional quenching process on the mesospheric OH emission layer: a study based on SD-WACCM4 and SABER, Atmos. Chem. Phys., 14, 10193-10210, https://doi.org/10.5194/acp-14-10193-2014, 2014.

Kulikov, M. Yu., and Feigin, A. M.: Reactive-diffusion waves in the mesospheric photochemical system. Adv. Space Res., 35(11), 1992-1998, https://doi.org/10.1016/j.asr.2005.04.020, 2005.

Kulikov, M. Y., Feigin, A. M., and Sonnemann, G. R.: Retrieval of the vertical distribution of chemical components in the mesosphere from simultaneous measurements of ozone and hydroxyl distributions, Radiophys Quantum El., 49, 683–691, https://doi.org/10.1007/s11141-006-0103-4, 2006.

Kulikov, M. Yu.: Theoretical investigation of the influence of a quasi 2-day wave on nonlinear photochemical oscillations in the mesopause region, J. Geophys. Res., 112, D02305, https://doi.org/10.1029/2005JD006845, 2007.

Kulikov, M. Y., Feigin, A. M., and Sonnemann, G. R.: Retrieval of water vapor profile in the mesosphere from satellite ozone and hydroxyl measurements by the basic dynamic model of mesospheric photochemical system, Atmos. Chem. Phys., 9, 8199–8210, https://doi.org/10.5194/acp-9-8199-2009, 2009.

Kulikov, M. Yu., Vadimova, O. L., Ignatov, S. K., and Feigin, A. M.: The mechanism of non-linear photochemical oscillations in the mesopause region, Nonlin. Processes Geophys., 19, 501–512, https://doi.org/10.5194/npg-19-501-2012, 2012.

Kulikov, M. Y., Belikovich, M. V., Grygalashvyly, M., Sonnemann, G. R., Ermakova, T. S., Nechaev, A. A., and Feigin, A. M.: Daytime ozone loss term in the mesopause region, Ann. Geophys., 35, 677-682 https://doi.org/10.5194/angeo-35-677-2017, 2017.

Kulikov, M. Y., Nechaev, A. A., Belikovich, M. V., Ermakova, T. S., and Feigin, A. M.: Technical note: Evaluation of the simultaneous measurements of mesospheric OH, HO_2, and O_3 under a photochemical equilibrium assumption – a statistical approach, Atm. Chem. Phys., 18, 7453-747, https://doi.org/10.5194/acp-18-7453-2018, 2018a.

Kulikov, M. Y., Belikovich, M. V., Grygalashvyly, M., Sonnemann, G. R., Ermakova, T. S., Nechaev, A. A., and Feigin, A. M.: Nighttime ozone chemical equilibrium in the mesopause region. J. Geophys. Res.,123, 3228–3242, https://doi.org/10.1002/2017JD026717, 2018b.

Kulikov, M. Yu., Nechaev, A. A., Belikovich, M. V., Vorobeva, E. V., Grygalashvyly, M., Sonnemann, G. R., and Feigin, A. M.: Border of nighttime ozone chemical equilibrium in the mesopause region from saber data: implications for derivation of atomic oxygen and atomic hydrogen, Geophys. Res. Lett., 46, 997–1004, https://doi.org/10.1029/2018GL080364, 2019.

Kulikov, M. Y., Belikovich, M. V., and Feigin, A. M.: Analytical investigation of the reaction-diffusion waves in the mesopause photochemistry, J. Geophys. Res., 125, e2020JD033480, https://doi.org/10.1029/2020JD033480, 2020.

Kulikov, M. Y., Belikovich, M. V., Feigin, A. M.: The 2-day photochemical oscillations in the mesopause region: the first experimental evidence? Geophys. Res. Lett., 48, e2021GL092795, https://doi.org/10.1029/2021GL092795, 2021.

Kulikov M. Yu., Belikovich, M. V., Grygalashvyly, M., Sonnemann, G. R., and Feigin, A. M.: Retrieving daytime distributions of O, H, OH, HO2, and chemical heating rate in the mesopause region from satellite observations of ozone and OH* volume emission: The evaluation of the importance of the reaction H+O3 $\rightarrow O_2$+OH in the ozone balance, Adv. Space Res., 69, 3362–3373,https://doi.org/10.1016/j.asr.2022.02.011, 2022a.

Kulikov, M. Y., Belikovich, M. V., Grygalashvyly, M., Sonnemann, G. R., and Feigin, A.M.: The revised method for retrieving daytime distributions of atomic oxygen and odd-hydrogens in the mesopause region from satellite observations, Earth Planets Space, 74, 44, https://doi.org/10.1186/s40623-022-01603-8, 2022b.

Kulikov, M. Yu., Belikovich, M. V., Chubarov, A. G., Dementeyva, S. O., Feigin, A. M.: Boundary of nighttime ozone chemical equilibrium in the mesopause region: improved criterion of determining the boundary from satellite data, Adv. Space Res., 71 (6), 2770-2780, https://doi.org/10.1016/j.asr.2022.11.005, 2023b.

Lawrence, Z. D., Perlwitz, J., Butler, A. H., Manney, G. L., Newman, P. A., Lee, S. H., Nash, E. R.: The remarkably strong Arctic stratospheric polar vortex of winter 2020: Links to record-breaking Arctic Oscillation and ozone loss, J. Geophys. Res. Atmos., 125, e2020JD033271, https://doi.org/10.1029/2020JD033271, 2020.

Liu, H.-L., Bardeen, C. G., Foster, B. T., Lauritzen, P., Liu, J., Lu, G., Marsh, D. R., Maute, A., McInerney, J. M., Pedatella, N. M., Qian, L., Richmond, A. D., Roble, R. G., Solomon, S. C., Vitt, F. M., Wang, W.: Development and validation of the Whole Atmosphere Community Climate Model with thermosphere and ionosphere extension (WACCM-X 2.0), J. Adv. Mod. Earth Sys., 10, 381–402, https://doi.org/10.1002/2017MS001232, 2018.

Llewellyn, E. J., McDade, I. C. Moorhouse, P., and Lockerbie, M. D.: Possible reference models for atomic oxygen in the terrestrial atmosphere, Adv. Space Res., 13, 135–144, https://doi.org/10.1016/0273-1177(93)90013-2, 1993.

Llewellyn, E. J., and McDade, I. C.: A reference model for atomic oxygen in the terrestrial atmosphere, Adv. Space Res., 18, 209–226, https://doi.org/10.1016/0273-1177(96)00059-2, 1996.

Lukianova, R., Kozlovsky, A., Lester, M.: Upper stratosphere-mesosphere-lower thermosphere perturbations during the formation of the Arctic polar night jet in 2019–2020, Geophys. Res. Lett., 48, e2021GL094926, https://doi.org/10.1029/2021GL094926, 2021.

https://doi.org/10.5194/egusphere-2026-4117
Preprint. Discussion started: 15 July 2026

Manney, G. L., Kruger, K., Sabutis, J. L., Sena, S. A., and Pawson, S.: The remarkable 2003–2004 winter and other recent warm winters in the Arctic stratosphere since the late 1990s. J. Geophys. Res., 110, D04107, https://doi.org/10.1029/2004JD005367, 2005.

Manney, G. L., Lawrence, Z. D., Santee, M. L., Read, W. G., Livesey, N. J., Lambert, A., Froidevaux, L., Pumphrey, H. C., and Schwartz, M. J.: A minor sudden stratospheric warming with a major impact: Transport and polar processing in the 2014/2015 Arctic winter, Geophys. Res. Lett., 42, 7808–7816, http://doi.org/10.1002/2015GL065864, 2015.

Marsh, D. R., Smith, A. K., Mlynczak, M. G., and Russell III, J. M.: SABER observations of the OH Meinel airglow variability near the mesopause, J. Geophys. Res., 111, A10S05, https://doi.org/10.1029/2005JA011451, 2006.

Matthias, V., Dörnbrack, A., and Stober, G.: The extraordinarily strong and cold polar vortex in the early northern winter 2015/2016, Geophys. Res. Lett., 43, 12287–12294, doi:10.1002/2016GL071676, 2016.

McDade, I. C., Llewellyn, E. J., and Harris, F. R.: Atomic oxygen concentrations in the lower auroral thermosphere, Adv. Space Res., 5, 229–232, https://doi.org/10.1029/GL011I003P00247, 1985.

McDade, I. C., and Llewellyn, E. J.: Mesospheric oxygen atom densities inferred from night-time OH Meinel band emission rates, Planet. Space Sci., 36, 897–905, https://doi.org/10.1016/0032-0633(88)90097-9, 1988.

Mlynczak, M. G., Marshall, B. T., Martin-Torres, F. J., Russell III, J. M., Thompson, R. E., Remsberg, E. E., and Gordley, L. L.: Sounding of the Atmosphere using Broadband Emission Radiometry observations of daytime mesospheric $O_2(^1D)$ 1.27 μm emission and derivation of ozone, atomic oxygen, and solar and chemical energy deposition rates, J. Geophys. Res., 112, D15306, https://doi.org/10.1029/2006JD008355, 2007.

Mlynczak, M. G., Hunt, L. A., Mast, J. C., Marshall, B. T., Russell III, J. M., Smith, A. K., Siskind, D. E., Yee, J.-H., Mertens, C. J., Martin-Torres, F. J., Thompson, R. E., Drob, D. P., and Gordley, L. L.: Atomic oxygen in the mesosphere and lower thermosphere derived from SABER: Algorithm theoretical basis and measurement uncertainty, J. Geophys. Res., 118, 5724–5735, https://doi.org/10.1002/jgrd.50401, 2013a.

Mlynczak, M. G., Hunt, L. H., Mertens, C. J., Marshall, B. T., Russell III, J. M., López-Puertas, M., Smith, A. K., Siskind, D. E., Mast, J. C., Thompson, R. E., and Gordley, L. L.: Radiative and energetic constraints on the global annual mean atomic oxygen concentration in the mesopause region, J. Geophys. Res. Atmos., 118, 5796–5802, https://doi.org/10.1002/jgrd.50400, 2013b.

Mlynczak, M. G., Hunt, L. A. Marshall, B. T. Mertens, C. J. Marsh, D. R. Smith, A. K. Russell, J. M. Siskind D. E., and Gordley L. L.: Atomic hydrogen in the mesopause region derived from SABER: Algorithm theoretical basis, measurement uncertainty, and results, J. Geophys. Res., 119, 3516–3526, https://doi.org/10.1002/2013JD021263, 2014.

Mlynczak, M. G., Hunt, L. A., Russell, J. M. III, and Marshall, B. T.: Updated SABER night atomic

https://doi.org/10.5194/egusphere-2026-4117
Preprint. Discussion started: 15 July 2026

oxygen and implications for SABER ozone and atomic hydrogen, Geophys. Res. Lett., 45, 5735–5741, https://doi.org/10.1029/2018GL077377, 2018.

Nikoukar, R., Swenson, G. R., Liu, A. Z., and Kamalabadi, F.: On the variability of mesospheric OH emission profiles, J. Geophys. Res., 112, D19109, https://doi.org/10.1029/2007JD008601, 2007.

Panka, P. A., Kutepov, A. A., Zhu, Y., Kaufmann, M., Kalogerakis, K. S., Rezac, L., Feofilov, A. G., Marsh, D. R., and Janches, D.: Simultaneous retrievals of nighttime O(3P) and total OH densities from satellite observations of Meinel band emissions, Geophys. Res. Lett., 48, e2020GL091053, https://doi.org/10.1029/2020GL091053, 2021.

Pendleton, W. R., Baker, K. D., Howlett, L. C.: Rocket-based investigations of $O(^3P)$, O_2 $(a^1\Delta_g)$ and OH* (v=1,2) during the solar eclipse of 26 February 1979, J. Atm. Terr. Phys., 45(7), 479-491, 1983.

Siskind, D. E., Marsh, D. R., Mlynczak, M. G., Martin-Torres, F. J., and Russell III, J. M.: Decreases in atomic hydrogen over the summer pole: Evidence for dehydration from polar mesospheric clouds? Geophys. Res. Lett., 35, L13809, https://doi.org/10.1029/2008GL033742, 2008.

Siskind, D. E., Mlynczak, M. G., Marshall, T., Friedrich, M., Gumbel, J.: Implications of odd oxygen observations by the TIMED/SABER instrument for lower D region ionospheric modeling, J. Atmos. Sol. Terr. Phys., 124, 63–70, https://doi.org/10.1016/j.jastp.2015.01.014, 2015.

Smith, A. K., Lopez-Puertas, M., Garcıa-Comas, M. and Tukiainen, S.: SABER observations of mesospheric ozone during NH late winter 2002–2009, Geophys. Res. Lett., 36, L23804, https://doi.org/10.1029/2009GL040942, 2009.

Smith, A. K., Marsh, D. R. Mlynczak, M. G. and Mast, J. C.: Temporal variations of atomic oxygen in the upper mesosphere from SABER, J. Geophys. Res., 115, D18309, https://doi.org/10.1029/2009JD013434, 2010.

Sonnemann, G., and Fichtelmann, B.: Enforced oscillations and resonances due to internal non-linear processes of photochemical system in the atmosphere, Acta. Geod. Geophys. Mont. Hung., 22, 301–311, 1987.

Sonnemann, G., and Fichtelmann, B.: Subharmonics, cascades of period of doubling and chaotic behavior of photochemistry of the mesopause region, J. Geophys. Res., 101, 1193-1203, https://doi.org/10.1029/96JD02740, 1997.

Sonnemann, G., Kremp, C. Ebel, A. and Berger U.: A three-dimensional dynamic model of minor constituents of the mesosphere, Atmos. Environ., 32, 3157–3172, https://doi.org/10.1016/S1352-2310(98)00113-7, 1998.

Sonnemann, G., Feigin, A. M., and Molkov, Ya. I.: On the influence of diffusion upon the nonlinear behaviour of the photochemistry of the mesopause region, J. Geophys. Res., 104, 30591-30603, https://doi.org/10.1029/1999JD900785, 1999.

Sonnemann, G., and Feigin, A. M.: Non-linear behaviour of a reaction-diffusion system of the

https://doi.org/10.5194/egusphere-2026-4117
Preprint. Discussion started: 15 July 2026

photochemistry within the mesopause region, Phys. Rev. E, 59, 1719-1726, https://doi.org/10.1103/PhysRevE.59.1719, 1999.

Sonnemann, G. R., and Grygalashvyly, M.: On the two-day oscillations and the day-to-day variability in global 3-D-modeling of the chemical system of the upper mesosphere/mesopause region, Nonlin. Processes Geophys., 12, 691– 705, https://doi.org/10.5194/npg-12-691-2005, 2005.

Sonnemann, G. R., Hartogh, P., Berger, U., and Grygalashvyly, M.: Hydroxyl layer: trend of number density and intra-annual variability, Ann. Geophys., 33, 749–767, https://doi.org/10.5194/angeo-33-749-2015, 2015.

Scinocca, J. F., McFarlane, N. A., Lazare, M., Li, J., and Plummer, D.: Technical Note: The CCCma third generation AGCM and its extension into the middle atmosphere, Atmos. Chem. Phys., 8, 7055–7074, https://doi.org/10.5194/acp-8-7055-2008, 2008.

Swenson, G. R., and Gardner C. S.: Analytical models for the responses of the mesospheric OH* and Na layers to atmospheric gravity waves, J. Geophys. Res., 103(D6), 6271–6294, https://doi.org/10.1029/97JD02985, 1998.

Thomas, R. J.: Atomic hydrogen and atomic oxygen density in the mesosphere region: Global and seasonal variations deduced from Solar Mesosphere Explorer near-infrared emissions, J. Geophys. Res., 95, 16,457–16,476, https://doi. org/ 10. 1029/ JD095 iD10p 16457, 1990.

Vincent, R. A., Kovalam, S., Reid, I. M., Murphy, D. J., Klekociuk, A.: Southern Hemisphere stratospheric warmings and coupling to the mesosphere-lower thermosphere J. Geophys. Res. Atmos., 127, e2022JD036558, https://doi.org/10.1029/2022JD036558, 2022.

Wang, L., Alexander, M. J.: Gravity wave activity during stratospheric sudden warmings in the 2007–2008 Northern Hemisphere winter, J. Geophys. Res., 114, D18108, http://doi.org/10.1029/2009JD011867, 2009.

Xu, J., Smith, A. K., Jiang, G., Gao, H., Wei, Y., Mlynczak, M. G., and Russell III, J. M.: Strong longitudinal variations in the OH nightglow, Geophys. Res. Lett., 37, L21801, https://doi.org/10.1029/2010GL043972, 2010.

Xu, J., Gao, H. Smith, A. K. and Zhu Y.: Using TIMED/SABER nightglow observations to investigate hydroxyl emission mechanisms in the mesopause region, J. Geophys. Res., 117, D02301, https://doi.org/10.1029/2011JD016342, 2012.

Yamazaki, Y., Sato, K., Koshin, D., Yasui, R., Atmospheric semidiurnal solar tide response to sudden stratospheric warmings in the JAGUAR-DAS Whole neutral Atmosphere Reanalysis (JAWARA) during 2004–2023, J. Geophys. Res. Sp. Phys., 130, e2024JA033688, https://doi.org/10.1029/2024JA033688, 2025.

Zi, Y., Long, Z., Sheng, J., Lu, G., Perrie, W., Xiao, Z.: The sudden stratospheric warming events in the Antarctic in 2024, Geophys. Res. Lett., *52*, e2025GL115257, https://doi.org/10.1029/2025GL115257, 2025.